






ORIGINAL PAPER

Open Access



Mid-Cretaceous extensional magmatism in the Alborz Mountains, north Iran; geochemistry and geochronology of Gasht-Masuleh gabbros

Leila Rezaei^{1,2*} , Martin J. Timmerman¹ , Mohssen Moazzen^{2,3}, Uwe Altenberger¹ , Jiří Sláma⁴ , Masafumi Sudo¹, Christina Günter¹, Franziska D. H. Wilke⁵  and Anja M. Schleicher⁵

Abstract

In the Gasht-Masuleh area in the Alborz Mountains, gabbroic magma intruded Palaeozoic metasediments and Mesozoic sediments and crystallised as isotropic and cumulate gabbros. LREE enrichment points to relatively low degrees of mantle melting and depletion of Ti, Nb and Ta relative to primitive mantle points to an arc related component in the magma. Clinopyroxene compositions indicate MORB to arc signatures. U–Pb zircon crystallisation ages of 99.5 ± 0.6 Ma and 99.4 ± 0.6 Ma and phlogopite $^{40}\text{Ar}/^{39}\text{Ar}$ ages of 97.1 ± 0.4 Ma, 97.5 ± 0.4 Ma, 97.1 ± 0.1 Ma, within 2 σ error, indicate that gabbro intrusion occurred in the (Albian-)Cenomanian (mid-Cretaceous). As active subduction did not take place in the Cretaceous in North Iran, the small volume mafic magmatism in the Gasht-Masuleh area must be due to local, extension-related mantle melting. Melting was most likely caused by far field effects triggered by roll-back of the Neo-Tethys subducting slab. As subduction took place at a distance of ~400 km (present distance) from the Alborz Mountains, the observed arc geochemical signatures must be inherited from a previous subduction event and concomitant mantle metasomatism, possibly in combination with contamination of the magma by crustal material.

Highlights

- Gasht-Masuleh gabbros calc-alkaline, extensional setting, inherited arc signature
- (Albian-) Cenomanian, 99 Ma zircon ages
- 97–98 Ma $^{40}\text{Ar}/^{39}\text{Ar}$ phlogopite ages
- Mantle upwelling and formation of gabbros triggered by Neo-Tethys slab roll-back causing extension

Keywords Gabbro, Mid-Cretaceous, Extension, Gasht-Masuleh, Alborz Mountains, North Iran

Handling editor: Paola Manzotti.

*Correspondence:

Leila Rezaei
rezaei@uni-potsdam.de

Full list of author information is available at the end of the article



© The Author(s) 2023. **Open Access** This article is licensed under a Creative Commons Attribution 4.0 International License, which permits use, sharing, adaptation, distribution and reproduction in any medium or format, as long as you give appropriate credit to the original author(s) and the source, provide a link to the Creative Commons licence, and indicate if changes were made. The images or other third party material in this article are included in the article's Creative Commons licence, unless indicated otherwise in a credit line to the material. If material is not included in the article's Creative Commons licence and your intended use is not permitted by statutory regulation or exceeds the permitted use, you will need to obtain permission directly from the copyright holder. To view a copy of this licence, visit <http://creativecommons.org/licenses/by/4.0/>.

1 Introduction

The two most important orogenies in Iran are related to the subduction and closure of the Palaeo- and Neo-Tethys Oceans in the late Triassic and late Cenozoic, respectively (e.g. Stampfli et al., 1991). Palaeo-Tethys closure was associated with accretion of Gondwana-derived Cimmerian terranes or micro-continents, such as the Central Iran micro-continent, to the southern margin of the Eurasian continent resulting in the approximately E-W trending Alborz orogen (Zanchi et al., 2009). Opening of the Neo-Tethys Ocean in the mid-Permian (Stampfli & Kozur, 2006) was followed by Late Triassic to Early Jurassic subduction initiation, the formation of a Jurassic-age magmatic arc (Hassanzadeh & Wernicke, 2016 and references therein), and late Oligocene–Miocene collision of Arabia forming the NW–SE trending Zagros orogen to the SW (Agard et al., 2011).

In the Alborz Mountains in the Late Triassic, extension associated with continental alkaline magmatic activity (e.g. Doroozi et al., 2016, 2018) was followed by deposition of shallow-marine siliciclastic rocks of the Late Triassic–Early Jurassic Shemshak Group. A continuous sequence of Early Jurassic to Cretaceous marine sediments overlies both basement rocks and the Shemshak Group with an unconformity that represents a long-lasting depositional hiatus (Fürsich et al., 2005).

Small volumes of mid-Cretaceous volcanic and plutonic rocks of intermediate to mafic composition and volcano-clastic sediments have been described in the central Alborz Mountains (Agard et al., 2011; Monsef et al., 2022), such as the Gasht-Masuleh gabbros (this study). In late Cretaceous times, thick sequences of limestones and carbonate-rich sediments were deposited in the

north–central Alborz. Late Palaeocene–Eocene extension-related volcanism was widespread in the Alborz Orogen (e.g. Karaj Formation, Asiabanha & Foden, 2012) as well as in the adjacent areas of Turkey, Armenia, Georgia and the Talesh Mountains in NW Iran, and was widespread, showing a large basic to acid, and sub-alkaline to alkaline compositional range.

Compared to the widespread and compositionally varied Palaeocene–Eocene volcanism (Verdel et al., 2011), magmatic rocks of Cretaceous age in the Alborz Mountains are rare and relatively small in volume. They are mostly exposed in the central Alborz Mountains, south-east of the Gasht-Masuleh area (Fig. 1). Rezaei et al. (2019, 2020) and Monsef et al. (2022) suggested that the Cretaceous, largely mafic magmas in the Alborz Mountains (and other regions such as the Iran-Armenia-Turkey Plateau; Monsef et al., 2022) were sourced from mantle material that was modified during subduction of the Palaeo-Tethys Ocean, and subsequently underwent fractional crystallisation. Mantle doming and far-field rift magmatism probably resulted from the Neo-Tethys subduction that affected Central Iran as far north as the South Caspian Basin (Monsef et al., 2022).

The occurrence of late Mesozoic mafic mantle-derived magmatic activity remote from active subduction zones and in an environment of quiet carbonate sedimentation raises questions about its age, source, cause and tectonic setting. This paper presents whole rock and mineral compositions, U–Pb zircon and $^{40}\text{Ar}/^{39}\text{Ar}$ phlogopite ages for gabbros in the Gasht-Masuleh area in order to determine the geochemical trends and tectonic setting of their magma. It focuses on the whole-rock composition of the isotropic gabbros (being the closest approximation

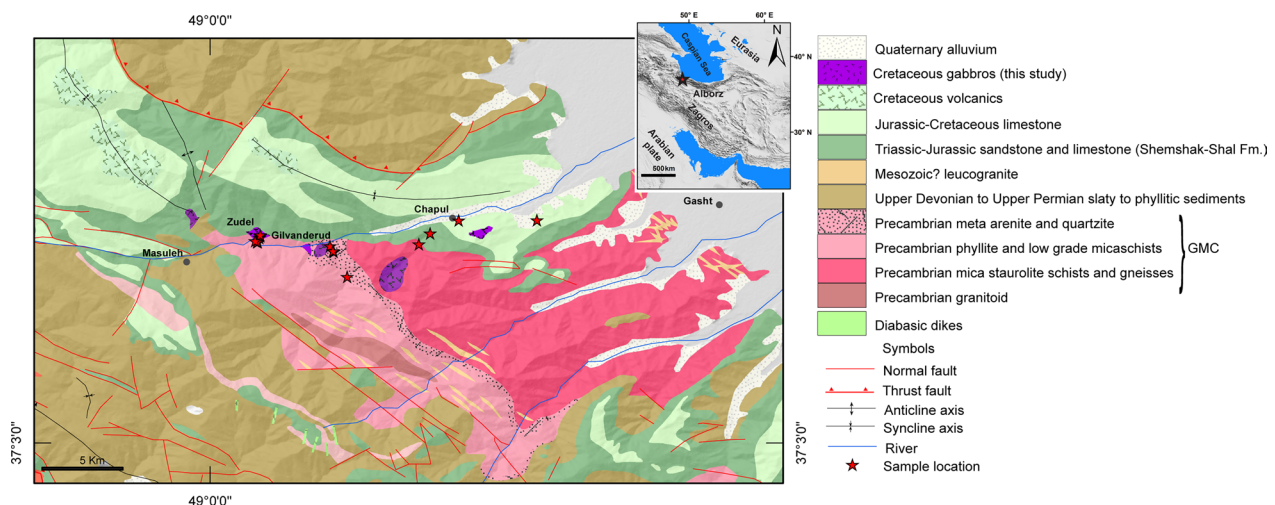


Fig. 1 Geological map of the Gasht-Masuleh area (simplified after Clark et al., 1975) showing sample locations. GMC = Gasht-Masuleh Metamorphic Complex

to magma) and mineral compositions of both isotropic and cumulate samples. In addition, their geochemistry is compared with published data from other Cretaceous mafic magmatic rocks in the Alborz Mountains in order to establish if they were derived from similar mantle sources and resulted from the same tectonic event(s).

2 Geological background

The Gasht-Masuleh area is located in the western Alborz Mountains to the west of Rasht city (Gilan, also Guilan, Province). Davies et al. (1972) and Clark et al. (1975) mapped the Masuleh area at the 1:100,000 scale and the Bandar-e-Anzali (formerly: Bandar-e-Pahlavi) area at the 1:250,000 scale. Later, the Geological Survey of Iran published the 1:100,000 scale map of the Bandar-e-Anzali area (Nazari et al., 2004).

The Alborz Mountains have a basement of predominantly metasediments of the Gasht Metamorphic Complex and small volumes of late Ediacaran granite (Hassanzadeh et al., 2008). The low-grade part of the Gasht Metamorphic Complex comprises phyllites, greenschist-facies metapelites and metasandstones with subordinate calc-silicates. The higher-grade part consists of amphibolite-facies metapelites (Fig. 1). Protolith sedimentation ages of the metasediments are probably Neoproterozoic (Clark et al., 1975). Amphibolite boulders in river-beds reveal the presence of nearby metabasites which, however, have not been found in exposure due to dense vegetation. The granite from Lahijan east of Rasht has a 551 ± 9 Ma U–Pb zircon age (Guest et al., 2006; hereafter, all age uncertainties are cited at 2-sigma level). In the Talesh Mountains in the West Alborz, lower Palaeozoic volcanic rocks occur interbedded with Silurian limestones and are overlain by Early Devonian limestones (Wendt et al., 2005; Zanchi et al., 2009).

In the study area, the Gasht Metamorphic Complex is overlain by unmetamorphosed Carboniferous black shales and Permian limestones and marls (Clark et al., 1975). The Late Triassic to Middle Jurassic (Bajocian) Shemshak Group overlies these rocks with an angular unconformity and mainly comprises shallow-marine siliciclastic rocks with coal bearing layers, changing to carbonates in Bajocian times (Fürsich et al., 2009). The unconformity is thought to be related to the closure of the Palaeo-Tethys Ocean and terrane accretion (Guest et al., 2006). The younger, mid- to late Jurassic Shal Formation consists of glauconitic and calcareous sandstones that were deposited in a shallow marine environment under oxidizing conditions. Shallow marine carbonates and volcanoclastic rocks of Cretaceous age cover the Jurassic formations (Clark et al., 1975). A granite that intrudes metamorphic basement rocks has an early Jurassic 180.5 ± 1.3 Ma U–Pb zircon crystallisation age (sample

AB422B of Chu et al., 2021). Further published U–Pb zircon ages are 99.1 ± 0.7 Ma for a small diorite intrusion in the western Gasht-Masuleh area (Chu et al., 2021), and 97.4 ± 1.8 Ma for the diorite phase and 96.9 ± 2.4 Ma for Nusha granite of a composite intrusion ESE of the Gasht-Masuleh area (Guest et al., 2006). Monsef et al., (2022) reported 99.6 ± 0.5 and 98.5 ± 0.7 Ma U–Pb zircon ages for Javaherdeh-Javaherdasht isotropic gabbros ~110 km to the E of Gasht-Masuleh and a 108.1 ± 1.4 Ma zircon U–Pb age for pillow lavas of the Shanderman-Asalem to the NW of the study area.

In the Gasht-Masuleh area, small, ca. 1.5 km² sized bodies of cumulates and isotropic gabbros are exposed near the villages of Zudel, Gilvanderud and Chapul (Fig. 1). These may be the exposed parts of a single, larger gabbro intrusion, but this remains conjectural due to the poor degree of exposure. Their magma intruded the basement metasediments and, locally, Shemshak Group and Shal Formation limestones and marls.

3 Gasht-Masuleh gabbro intrusions

The gabbros are coarse- to medium-grained clinopyroxene-olivine to plagioclase-rich cumulates and isotropic gabbros. Compared to the isotropic gabbros, the cumulate gabbros volumetrically predominate in the study area. Due to the dense vegetation cover, extensive weathering and thick soil in the area, contacts between gabbros and host rocks are not exposed. Large, loose and locally-derived blocks of the Chapul intrusion in the main valley dissecting the western part of the body are clinopyroxene- and olivine-rich cumulates (Fig. 2A). The Gilvanderud intrusion cuts metasediments of the Gasht Metamorphic Complex and consists of coarse- to medium-grained isotropic gabbros and coarse-grained clinopyroxene-olivine cumulates. The intrusion is crosscut by centimetre to decimetre thick dolerite and diorite dykes (Fig. 2B). The Zudel gabbro intruded the Gasht Metamorphic Complex and sediments of the Shemshak Group and Shal Formation. It consists of coarse-grained isotropic gabbros, and of plagioclase-rich cumulates showing modal layering of plagioclase-rich light-coloured layers and dark-coloured layers composed of pyroxene, phlogopite and opaque minerals (Fig. 2C). The gabbros are crosscut by undated dolerite, diorite dykes and fine-grained gabbro dykes of up to 50 cm thick.

Magmatic textures (e.g. layering) and minerals are well preserved and the rocks are not metamorphosed or folded. Brittle deformation and faulting locally resulted in the formation of slickensides on fault planes and tilting of the magmatic layering, the latter feature is especially clear in the Zudel intrusion (Fig. 2D). These features indicate that the intrusions were affected by younger active

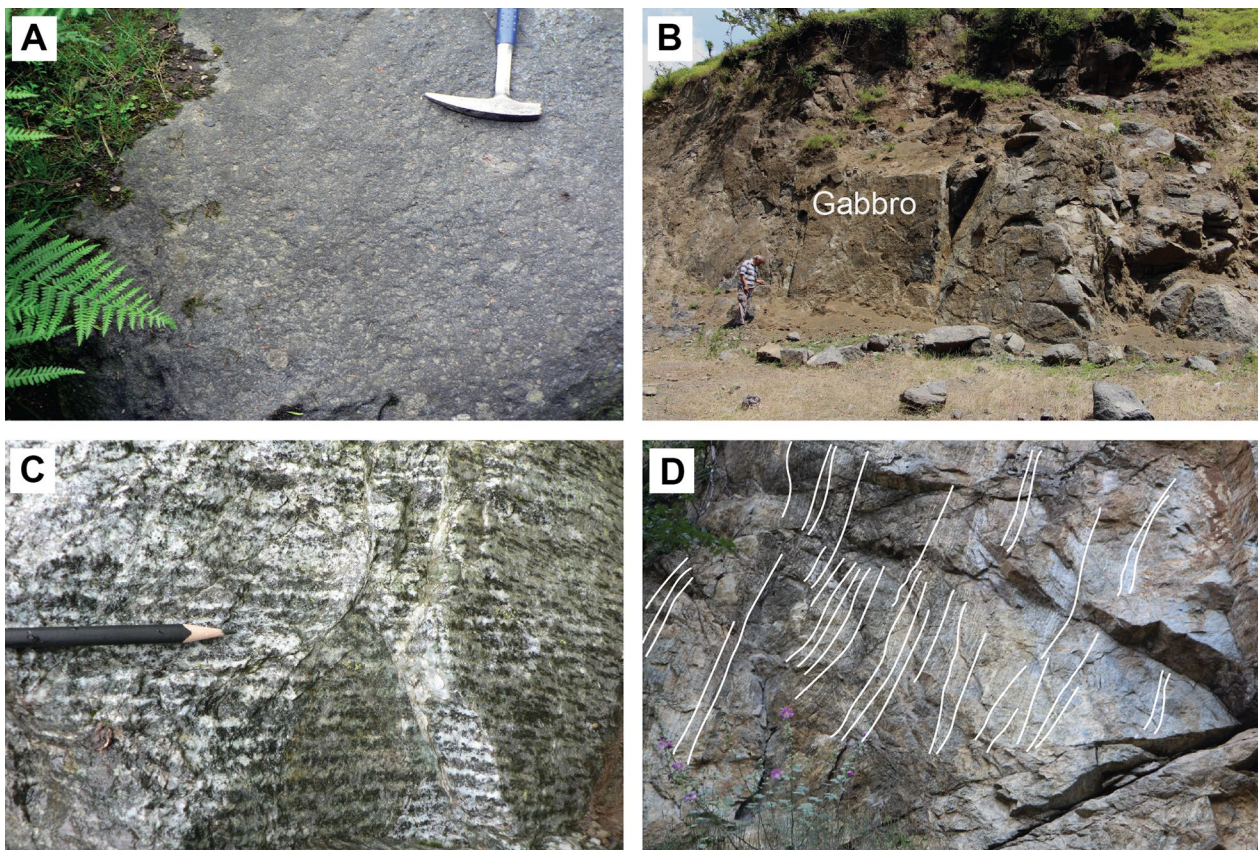


Fig. 2 Field photographs of the Gasht-Masuleh gabbros, **A** Cumulate gabbro from the Chapul intrusion. **B** Typical exposure of gabbros of the Gilvanderud intrusion, the gabbros are jointed and weathered on the surface. **C** Hand specimen of plagioclase-rich gabbro from the Zudel intrusion showing modal magmatic layering, with accumulation of plagioclase in the light layers and of mainly clinopyroxene, phlogopite and Fe-Ti oxides in dark layers. **D** Gabbro of the Zudel intrusion with tilted modal magmatic layering (highlighted by white lines)

tectonic events probably during the exhumation of the rocks during the Cenozoic.

The gabbros were considered to be Palaeozoic in age because they intruded the Gasht Metamorphic Complex (Nazari et al., 2004). However, map information indicates that the gabbros intruded Jurassic sediments showing that they must have Jurassic or younger crystallisation ages (Fig. 1). Field relations between the gabbros and the early Jurassic granites are unknown because of lack of exposure.

4 Petrography

The Gasht-Masuleh gabbros are mainly coarse-grained grey gabbros with isotropic and cumulate textures. The petrography of the cumulate samples is described in Additional file 1; this study focuses on the isotropic gabbros. Samples with ophitic texture are medium- to coarse-grained and contain clinopyroxene up to 2 mm (30–40 vol%), euhedral to subhedral laths of plagioclase up to 1 mm (30–50 vol%), olivine up to 0.5 mm (5–10 vol%), phlogopite (5–10 vol%) up to 1 mm in diameter,

and magnetite-ilmenite exsolutions (5–10 vol%) and accessory apatite (up to 2 vol%) (Fig. 3A). Orthopyroxene is rare and occurs as small grains on olivine rims and between olivine and clinopyroxene, and as inclusions in clinopyroxene. The approximate crystallisation order is olivine → olivine ± orthopyroxene → clinopyroxene → plagioclase ± clinopyroxene → opaque mineral(s) → phlogopite (based on petrographic observation listed in Additional file 8). Phlogopite is present as late anhedral grains, as rims overgrowing opaque minerals, and as anhedral patches locally replacing clinopyroxene crystal margins. Clinopyroxene rims partially reacted to brown and green amphibole; phlogopite and amphibole appear in micro-fractures in clinopyroxene. Olivine is partially altered to serpentine and iddingsite developing along cracks and at the rims. Phlogopite in some samples is altered to secondary unidentified opaque minerals and chlorite along cleavages and at the rims.

Opaque minerals in gabbro samples of especially the Zudel body are inhomogeneous and show extensive evidence of magnetite-ilmenite exsolution (Fig. 3B).

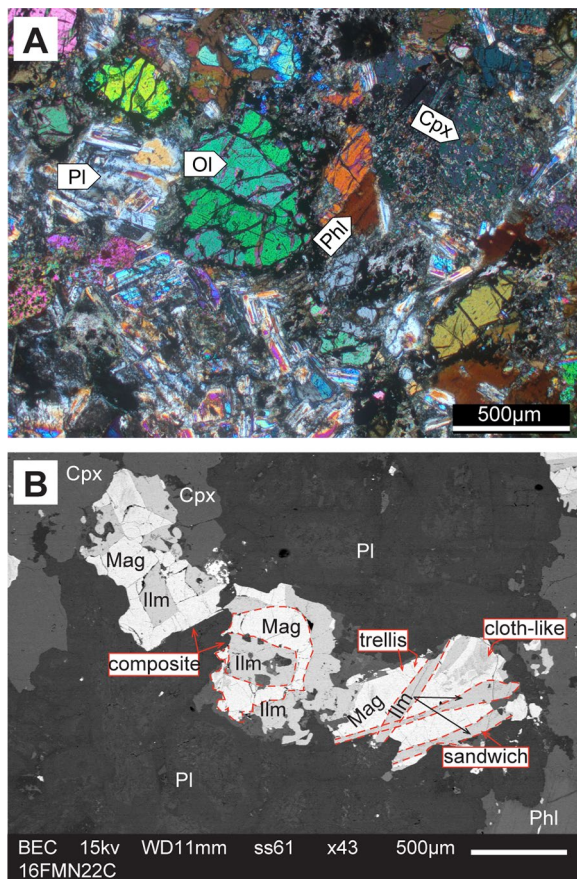


Fig. 3 **A** Photomicrographs (crossed nicols) of samples of Gasht-Masuleh isotropic gabbro sample 16FMN22D with ophitic texture from Zudel intrusion. **B** Back-scattered electron image of Fe-Ti oxides in sample 16FMN22C of the Zudel intrusion showing textures of *trellis* type: thin ilmenite spindles in magnetite displaying sharp contacts with the magnetite host, *sandwich* type: thick, lath-shaped ilmenite lamellae in magnetite with sharp mutual boundaries, *composite* type: aggregates in which ilmenite surrounds or is partly included in magnetite with sharp contact, and *cloth-like to graphic and vermicular*: fine-grained exsolutions of anhedral ilmenite and magnetite. Mineral name abbreviations in the text, tables and figures are after Whitney and Evans, (2010)

The amount of opaque minerals is low, ranging between absent to 5 vol%, in some samples reaching 10 vol%. In some samples from the Zudel and Gilvanderud intrusions they are relatively large and range from 0.2 to 1 mm. The largest grains are found in plagioclase-rich gabbros, all from the Zudel body. The exsolution textures as observed in back-scatter electron images can be divided into four major textural types following Buddington and Lindsley (1964) and Haggerty (1991) (see the figure caption for the textural types).

5 Methods and materials

The analytical methods are described in detail in Additional file 1, which also specifies the instrumental parameters, experimental conditions, reference materials, data reduction methods and plateau criteria. 18 samples were processed for whole rock major (XRF) and trace element (ICP-OES, ICP-MS) analyses. Wavelength-dispersive electron probe microanalyses (EPMA) were carried out on olivine, ortho- and clinopyroxene, plagioclase and phlogopite in 9 samples. Ce, Pr, Nd, Sr and Sc concentrations of clinopyroxenes, Ba, Rb, F and Cl concentrations in phlogopites, and Rb, Ba, Sr and Eu concentrations of plagioclases in selected samples were determined by field-emission microprobe. Zircons from one isotropic gabbro sample and one gabbroic cumulate sample, and phlogopite from three cumulate samples of isotropic gabbro and gabbroic cumulate were dated by LA-ICP-MS on zircon and $^{40}\text{Ar}/^{39}\text{Ar}$ step-heating of phlogopite.

6 Results

6.1 Whole rock geochemistry

Since the whole rock chemistry of cumulates is controlled by modal proportions of cumulate minerals and not by melt, we only focus on the chemistry of isotropic gabbros, considering these to be the closest representative of magma compositions. These we compared with the chemistry of other mid-Cretaceous basic magmatic rocks in the west Alborz Mountains, especially the basalts from Abrud village in the Gasht-Masuleh area (Rezaei et al., 2020) and the Talesh-Lahijan basaltic lavas (Monsef et al., 2022).

Whole rock major oxides and selected trace elements for the isotropic gabbros (including rare earth element, REE) concentrations are given in Additional file 2: Table S2. SiO_2 contents are 42.2–47.8 wt% and MgO (3.9–12.6 wt%), TiO_2 (0.5–2.8 wt%), FeO^t (6.0–16.1 wt%), Al_2O_3 (10.5–18.0 wt%), CaO (10.4–19.2 wt%), Na_2O (0.2–2.7 wt%) and K_2O (0.7–1.5 wt%) show variable ranges. Whole rock Mg# show a considerable range from 38.7 to 76.6 and LOI values vary between 1.2 to 3.4 wt%.

Figure 4A–I shows the variation diagrams for whole rock SiO_2 , Al_2O_3 , CaO, FeO^t , TiO_2 , Na_2O , Sr, Ni and Zr concentrations against MgO as fractionation index. They show that SiO_2 concentrations stay within the narrow range of 41–48 wt% whereas CaO increases and Al_2O_3 , TiO_2 and Na_2O decrease with increasing MgO. FeO^t shows no recognizable correlation and, except two samples (16FMN48B and 16FMN70A). Sr, Zr contents decrease and Ni increases with increasing MgO. The Gasht-Masuleh gabbros do not show distinct compositional differences from the basalts from Abrud and Talesh-Lahijan areas.

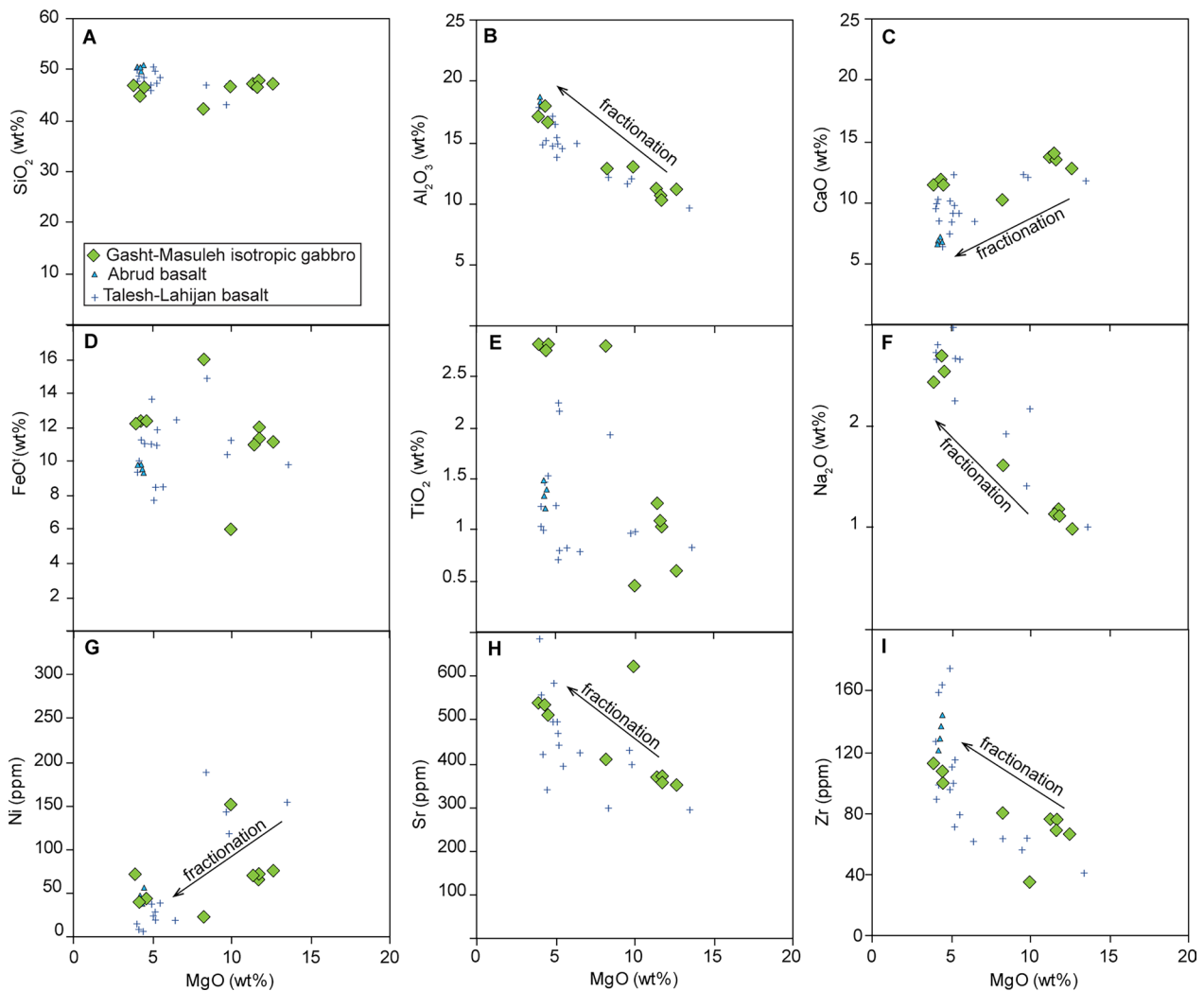


Fig. 4 A–I Variation diagrams of MgO vs. SiO_2 , Al_2O_3 , CaO, FeO, TiO_2 , Na_2O , Ni, Sr and Zr for the Gasht-Masuleh gabbros. The chemistry of the gabbros is compared with the basalts from Abrud (Rezaei et al., 2020) and Talesh-Lahijan (Monsef et al., 2022)

Chondrite normalised rare earth elements (REE) patterns show moderate LREE enrichment (Fig. 5A). Apart from Eu, patterns for all samples are sub-parallel, showing similar trends to bulk continental crust of Rudnick and Gao (2003) and plot below the oceanic island basalt (OIB) values of Sun and McDonough (1989). Compared to N-MORB (Sun & McDonough, 1989) the gabbros are enriched in LREE and depleted in HREE. $(\text{La}/\text{Yb})_{\text{N}}$ vary from 3.9 to 7.9, overlapping those of the Abrud and Talesh-Lahijan basalts. $(\text{La}/\text{Sm})_{\text{N}}$ vary from 1.2 to 2.6 and $(\text{Dy}/\text{Yb})_{\text{N}}$ vary from 1.4 to 1.8 in the samples. Europium anomalies ($\text{Eu}_{\text{N}}/\text{Eu}^*$) are absent to weakly negative in most samples (0.8–1.0), and slightly more negative in sample 16FMN22C-2 (0.8).

Total REE concentrations are 30–123 ppm with total LREE (La–Nd) concentrations of 13–69 and total HREE

(Sm–Lu) concentrations of 6–22 times chondrite (Additional file 2). $\text{La}_{\text{N}} = 16\text{--}89$ and $\text{Yb}_{\text{N}} = 4\text{--}12$.

The primitive mantle normalised multi-element patterns (Fig. 5B) are sub-parallel and resemble that of OIB, except that some samples have higher Rb, Ba and K concentrations. Nb, Ta, P and Ti are generally depleted causing negative anomalies to varying degrees.

6.2 Mineral chemistry

Selected analyses of olivine, orthopyroxene, clinopyroxene, plagioclase and phlogopite are listed in Additional file 3, Additional file 4, Additional file 5, Additional file 6 and Additional file 7, respectively.

6.2.1 Olivine

Individual crystals lack compositional variations from rim to core and are mainly homogenous. Olivine in

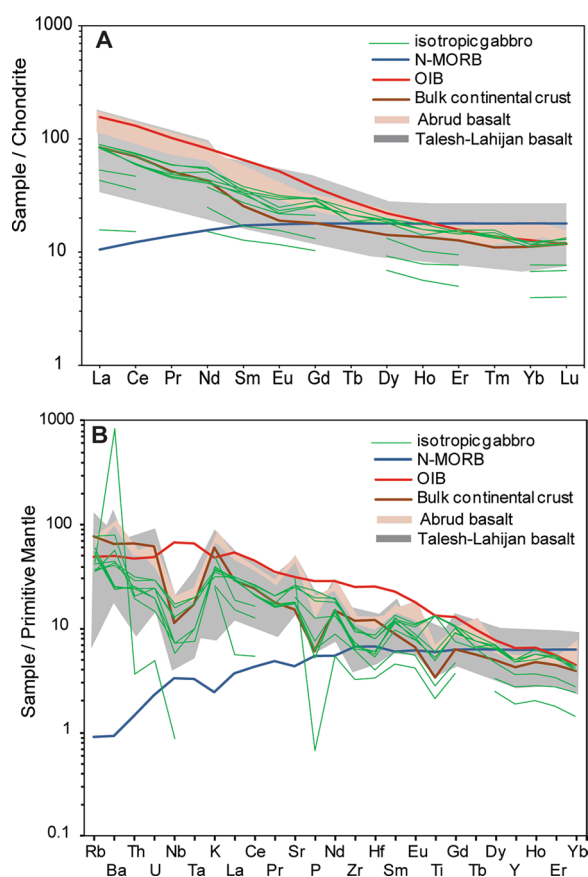


Fig. 5 **A** Chondrite normalised rare earth element patterns of the Gasht-Masuleh isotropic gabbros showing moderate LREE enrichment compared to the HREE. **B** Primitive Mantle normalised multi-element pattern of the gabbros overlapping the bulk continental crust composition. REE and multi-element patterns from the Abrud (Rezaei et al., 2020) and Talesh-Lahijan (Monsef et al., 2022) areas are plotted for chemical comparison. Chondrite and Primitive Mantle normalisation values, and OIB and N-MORB are from Sun and McDonough, (1989); bulk continental crust values are from Rudnick and Gao, (2003)

cumulate samples is relatively magnesium-rich with Mg# between 69.1 and 75.3, compared to olivine in isotropic gabbros (65.7–69.5). NiO contents are very low and range from below detection limit to 0.16 wt% in both cumulates and isotropic gabbros, and do not correlate with forsterite (Fo) content. Cr₂O₃ abundances are below 0.03 wt% in all olivine-bearing samples. MnO ranges between 0.28 and 0.61 wt% and shows a slight inverse correlation with Fo contents. Olivine in cumulate samples has Fo_{68.7–75}, whereas Fo_{65–69.1} in isotropic gabbros. Furthermore, Fo component in all samples is lower than those in mantle peridotites (Fo > 83%, Taka-hashi, 1986). Olivine in Chapul cumulate samples is richer in Fo_{71.9–75} compared to those in the Gilvanderud and Zudel cumulates (71.1–73.4% resp. 68.7–72.2%).

6.2.2 Orthopyroxene

Orthopyroxene is rare and appears at the rims of olivine and rarely as individual grains. Orthopyroxenes in cumulate gabbros is slightly richer in Mg (Mg# 73.2–76.9) and Al (0.2–1.5 wt% Al₂O₃) than those in isotropic samples (Mg# 64.7–74.8; 0.1–1.2 wt% Al₂O₃), but CaO contents in both cumulate and isotropic samples are similar (0.2–1.3 wt%). Orthopyroxene end-member (wollastonite, enstatite and ferrosilite) compositions are Wo_{0.4–2.5}En_{73.8–78.9}Fs_{19.7–24.7} in cumulate samples, and Wo_{0.5–2.6}En_{63.3–76.4}Fs_{22.6–34.1} in isotropic samples (calculated following Howie et al., 1992). They are enstatite according to the classification of Morimoto, (1988) (Additional file 4).

6.2.3 Clinopyroxene

Mg# of clinopyroxene in cumulate samples varies between 67.4 and 92.3, and in isotropic gabbros between 69.3 and 91.5 (Additional file 5: Table S5). Clinopyroxene in cumulate samples comprises Wo_{41.2–51.6}En_{41.1–51}Fs_{0.9–12.7} end member component, whereas clinopyroxene in isotropic gabbros contains Wo_{42.5–50.5}En_{37.5–49.9}Fs_{2.4–16.5}. Clinopyroxene in plagioclase-bearing cumulate samples has higher amounts of Fs compared to those in olivine-bearing cumulates. Clinopyroxene in all three intrusions lacks significant compositional major and trace element zoning. They are diopside to augite according to the classification of Morimoto (1988).

6.2.4 Plagioclase

Plagioclase in most samples is altered to various degrees, and only unaltered parts were analysed. Plagioclase in both cumulate and isotropic samples has similar compositions and is zoned. Anorthite (An) end-member contents range widely from very low 7.1 (probably secondary plagioclase) to 89.2 mol% for cumulate and 11.8 to 92.4 mol% for isotropic samples, with cores having high and rims low An contents. Selected trace element concentrations for plagioclases in three cumulate and two isotropic samples are at or just above detection limits: <0.02–0.1 wt% Rb₂O, <0.04–0.1 wt% BaO, 0.1–0.3 wt% SrO and <0.03–0.3 wt% Eu₂O₃. Sr and Ba concentrations for low-An rims and high-An cores in both cumulate and isotropic samples overlap and do not correlate with the respective anorthite end-member compositions, but Rb concentrations in rims are at or below the detection limit, and Eu concentrations at the rims are lower on average than in cores.

6.2.5 Phlogopite

Phlogopites generally have high TiO₂ contents of up to 7.6 wt% and high MgO contents of up to 23.9 wt%. CaO

contents reach 0.2 wt% (K_2O contents vary from 6.8 to 9.9 wt%. Mg# for phlogopite in cumulates are 53.0–85.0, and 60.7–83.3 in isotropic gabbros. Many phlogopites are enriched in Cl (0.1–0.4 wt% in cumulates and 0.2–0.5 wt% in isotropic gabbros) and F (up to 0.3 wt% in cumulates and up to 0.2 wt% in isotropic gabbros). Phlogopites in samples 16FMN45A and 16FMN20A that were dated by $^{40}Ar/^{39}Ar$ step-heating show no evidence for Ti, Mg, K and Fe compositional zoning.

6.3 Geochronology

6.3.1 LA-ICP MS U–Pb zircon dating results

Two samples, a cumulate (15FMN06) and an isotropic gabbro (GH 16–77) were chosen for LA-ICP-MS U–Pb zircon dating. Samples descriptions are given in Additional file 8. The dated zircons are colourless, mainly euhedral long prismatic crystals of up to 100 μm long and ~ 50 μm wide. Some crystals are fragmented due to sample processing. In CL images most crystals show concentric growth zoning typical for magmatic zircons (Fig. 6A, B). U concentrations vary from 174 to 3002 ppm, Th concentrations from 85 and 8764 ppm, and Th/U ratios range from 0.1 to 11.2 ppm. Analysis number (gh1677_13) displays a Th content of 22280 ppm and U content of 3790 ppm, suggesting it is a potential outlier. These concentrations may be analytical artefacts or due to heterogeneity of the zircon grain. However, the Th, U

and Pb concentrations of analysis gh1677-13 do not have a significant influence on the calculated age. For the calculation of Concordia ages, only analyses that are 2% or less discordant were used. The analytical data, the ranked and weighted ^{238}U – ^{206}Pb age average plots, the Concordia diagrams with all analysed points, and the data reporting sheet are given in Additional file 9.

Leucocratic gabbro 15FMN06 (Zudel) yielded thirteen spot ages, of which one is 14.9% discordant and has a 101 Ma $^{206}Pb/^{238}U$ age (X15fmn06_5). Of the thirteen analyses, twelve that are <2% discordant were used to calculate a Concordia age of 99.5 ± 0.6 Ma (Fig. 6A). Isotropic gabbro GH 16–77 (Gilvanderud) yielded fourteen spot ages of which four (grains 1, 3, 10 and 12) were more than 2% discordant. Two further analyses are 8.1 and 8.2% discordant and have $^{206}Pb/^{238}U$ ages of 104 resp. 101 Ma (gh1677_10 and _3). Ten, <2% discordant analyses yield a Concordia age of 99.4 ± 0.6 Ma (Fig. 6B). One grain yielded a 119 Ma age that was 66% discordant and not included in the age calculation (analysis gh1677_12, Additional file 9).

6.3.2 $^{40}Ar/^{39}Ar$ phlogopite step-heating dating results

Step-heating dating of magmatic phlogopite of three cumulate gabbro samples yielded plateau ages on 2-sigma level for samples 16FMN20A (Zudel) and 16FMN45A (Gilvanderud), but the age spectrum of

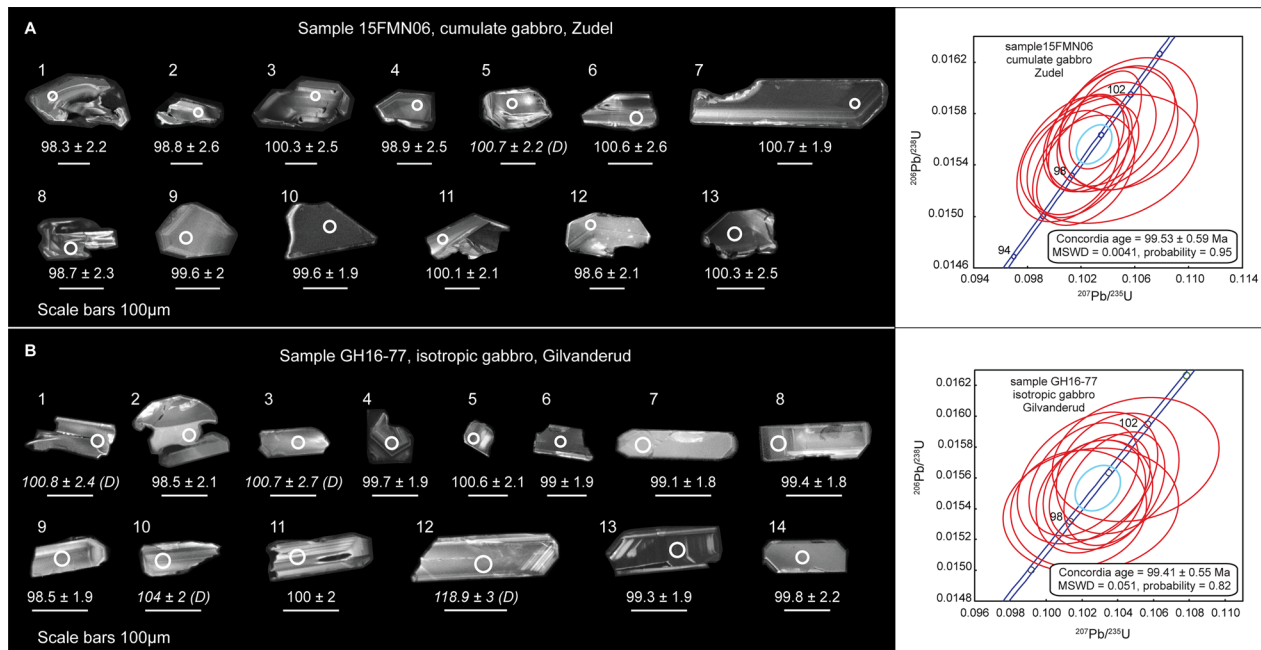


Fig. 6 Cathodoluminescence images and Concordia diagrams of magmatic zircons from the Gasht-Masuleh gabbros **A** Cumulate gabbro 15FMN06 of the Zudel intrusion. **B** isotropic gabbro GH16-77 of the Gilvanderud intrusion. The spots where laser-ablation analyses were performed are labelled with spot number and $^{206}Pb/^{238}U$ ages. Data-point error ellipses are 2σ . (D) denotes the analyses that are more than 2 percent discordant

sample 15FMN05A (Chapul) only allowed calculation of a forced plateau age. $^{40}\text{Ar}/^{39}\text{Ar}$ step-heating data including uncertainties are given in Additional file 10. Phlogopite 16FMN20A (Zudel) yielded a 97.1 ± 0.4 Ma plateau age for five gas fractions 8 to 12 comprising 69% of the total ^{39}Ar released (Fig. 7A), similar to the 97.2 ± 0.4 Ma total gas age. Phlogopite 16FMN45A (Gilvanderud) yielded a 97.5 ± 0.4 Ma plateau age for six gas fractions 4 to 9 comprising 94% of the ^{39}Ar released (Fig. 7B), which is indistinguishable from the 97.7 ± 0.4 Ma total gas age. In contrast, apparent ages for 15FMN05A (Chapul) did not yield a plateau age, but noting that gas fractions 4 to 10 have apparent ages that are similar (between 94.7 Ma and 98.9 Ma) and almost within 4 Ma of each other, comprising 95% of the ^{39}Ar released. However, the longest continuous steps which agree within 2-sigma error by their internal errors (excluding common J value errors) were only obtained for steps 5 to 6 (comprising 34% of the ^{39}Ar released). These steps are here named a forced plateau, which does not satisfy the typical criteria of the plateau that should comprise more than 50% of the ^{39}Ar released. The weighted mean age calculated from these forced plateau steps is 97.1 ± 0.1 Ma. This forced plateau age is indistinguishable from the 97.2 ± 0.4 Ma total gas age (Fig. 7C) and both ages also overlap the plateau ages of samples 16FMN20A and 16FMN45A within 1-sigma.

7 Discussion

7.1 Petrography and crystallisation sequence

The crystallisation sequence of the gabbros is olivine, present as isolated individual crystals or as inclusions in clinopyroxene, followed by clinopyroxene, and clinopyroxene and plagioclase. Fe-Ti oxides occur both as inclusions in phlogopite and clinopyroxene, and as individual grains. Phlogopite appears as the latest phase as both subhedral to anhedral crystals, overgrows Fe-Ti oxides and locally replaces clinopyroxene.

The textural varieties of the Fe-Ti oxides (Fig. 3B) indicate a cooling history under oxidizing conditions of an originally homogeneous magmatic Fe-Ti phase, such as ulvöspinel-rich magnetite. Trellis, sandwich and composite textures are super-solvus exsolution textures that formed at temperatures above the magnetite-ulvöspinel solvus, whereas cloth-like to graphic and vermicular textures formed at sub-solvus conditions (Buddington & Lindsley, 1964). Furthermore, crystallisation of an OH-bearing magmatic mineral such as phlogopite points to elevated water contents of the magma during the final stages of crystallisation. We suggest that, following crystallisation and (in cumulate samples) gravitational settling of a homogenous Fe-Ti oxide phase, the trellis, sandwich and composite type textures developed upon cooling of the rocks to temperatures of 800–850 °C (e.g.

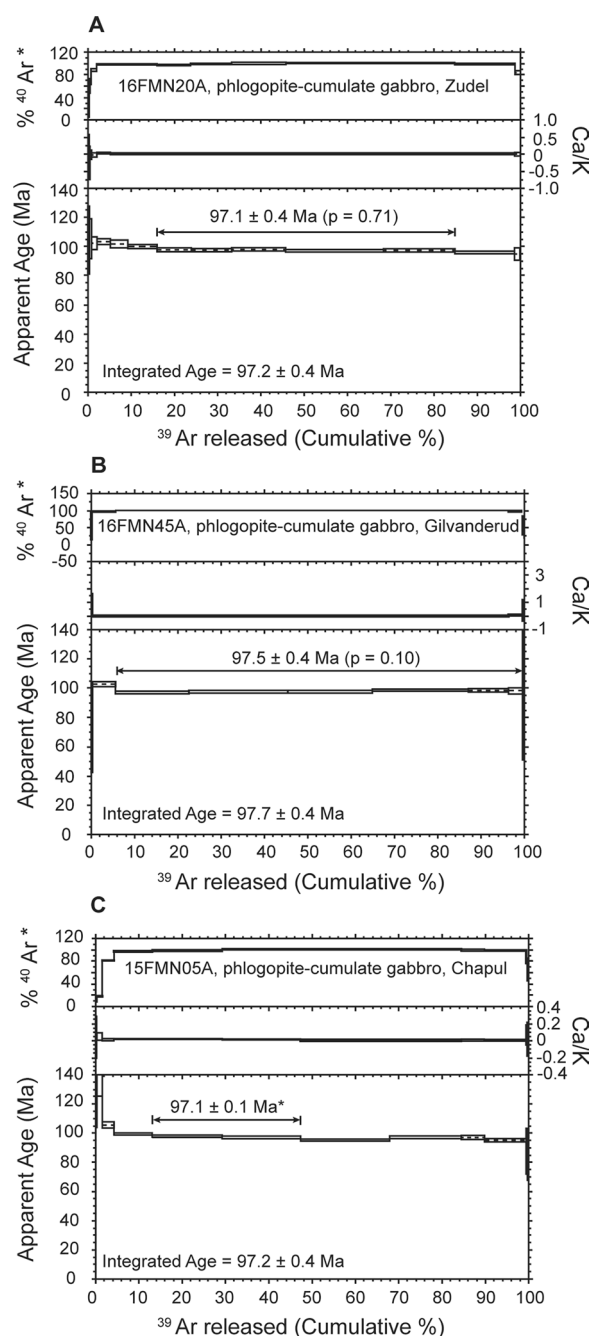


Fig. 7. $^{40}\text{Ar}/^{39}\text{Ar}$ incremental step heating age spectra, Ca/K ratios and fractions (%) of the radiogenic ^{40}Ar of magmatic phlogopite of cumulate samples **A** 16FMN20A (Zudel intrusion) and **B** 16FMN45A (Gilvanderud intrusion) yielding plateau ages. **C** A forced plateau age (*) for 2 gas fractions of step 5–6 was calculated for phlogopite from 15FMN05A (Chapul intrusion)

Buddington & Lindsley, 1964) in the presence of small amounts of H_2O -rich fluids. The fine-grained character of the minerals involved in the cloth-like ilmenite-magnetite

exsolutions indicate formation during increased cooling rates at lower temperatures.

7.2 Whole rock compositions

The MgO contents of the isotropic gabbros are between 3.9 and 12.6 wt%. This also explains the dominantly linear trends in the variation diagrams that lack inflections (Fig. 4A–I). The variation diagrams show that Al_2O_3 and Na_2O decrease and CaO increases with increasing MgO concentrations, overall indicating fractional crystallisation of clinopyroxene before plagioclase. Samples with low MgO have an elevated TiO_2 concentrations caused by the presence of large phlogopite crystals and (especially for the Zudel intrusion) magnetite-ilmenite exsolutions. Ni concentrations increase with increasing MgO due to the presence olivine. Like Al_2O_3 , Sr concentrations decrease with increasing MgO in gabbros reflecting fractionation of plagioclase. The major oxides and trace element compositions of the isotropic gabbros overlap with the compositions of basalts from Abrud and Talesh-Lahijan areas.

The multi-element patterns for the Gasht-Masuleh isotropic gabbros overlap that of bulk continental crust of Rudnick and Gao (2003) (Fig. 5A). Compared to primitive mantle, the samples are enriched in LILE (Ba, Rb, K) and depleted in HFSE (Nb, Ta, Zr, Ti and P in Fig. 5B) which points to a subduction-related component, the influence of slab derived fluids in their mantle source, and possibly to contamination of magma by continental crust and/or low degree of mantle melting. Generally, the patterns

gently slope from Rb to Yb, and show positive and negative anomalies. Nb and Ta depletions seen in many of the samples point to magma generation in an arc-related setting, or their contamination by continental crust (White & Patchett, 1984), or may be a feature inherited from the mantle source (see Discussion below). Ti depletion may be a primary feature of the mantle source, but can also be due to removal of Fe-Ti oxides during fractionation.

REE and trace elements are considered to describe the character of the of Gasht-Masuleh gabbro magma. In the Nb/Y vs. Ti/Y diagram of Pearce, (1982) the samples trend from the low Ti and low Nb mid-ocean ridge fields to the volcanic arc field together with the basalts from Abrud and Talesh-Lahijan areas, having sub-alkaline Nb/Y ratios < 1 (Fig. 8A).

Nb/La ratios of the isotropic gabbros are lower than those for MORB and OIB (0.2–0.7) suggesting a lithospheric mantle source, and/or contributions by lithospheric and asthenospheric mantle to the Gasht-Masuleh gabbros (Fig. 8B; Smith et al., 1999).

Isotropic gabbros and the basalts from the West Alborz (here compared samples from Abrud and Talesh-Lahijan areas) show a transitional magma character between tholeiitic and calc-alkaline to calc-alkaline magmas on the Zr/Y vs. Th/Yb magmatic affinity diagram of Ross and Bédard, (2009) (Fig. 9A). Zr, Nb, and Y contents are useful in identifying the source components of the magma (Condie, 2003, 2005; Fitton et al., 1997; Smith et al., 1999). Zr/Nb values range from 9 to 19 the Gasht-Masuleh gabbros (except for sample 16FMN48B with

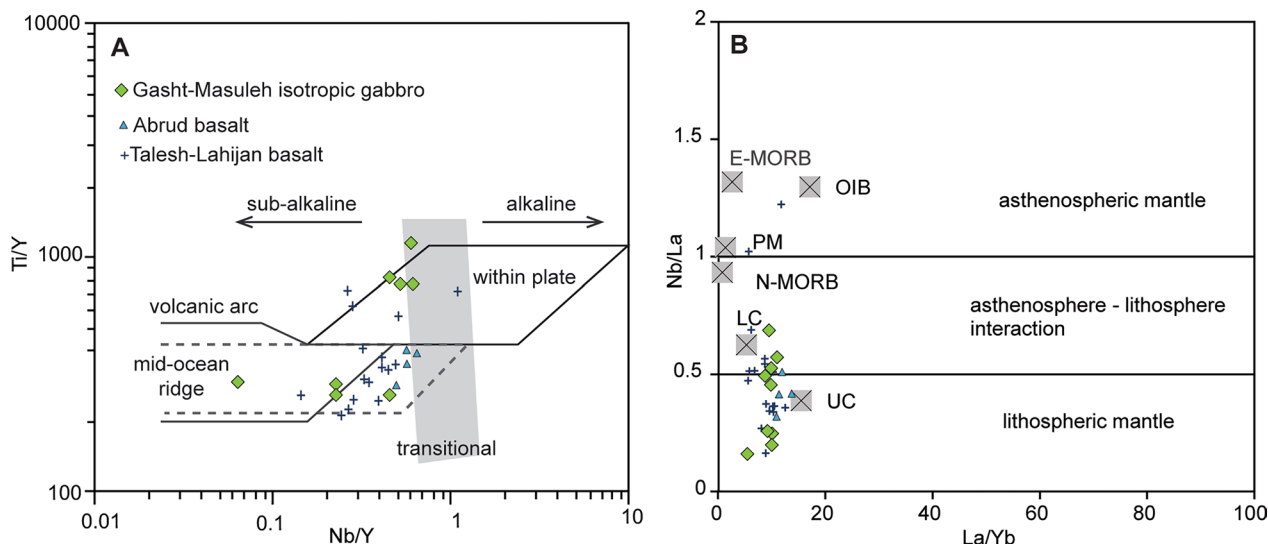


Fig. 8 **A** Nb/Y vs. Ti/Y diagram of Pearce, (1982), Nb/Y ratios (grey area) taken from Winchester and Floyd, (1977). **B** La/Yb vs. Nb/La plot, indicating a lithospheric mantle source contribution to the magma of the Gasht-Masuleh gabbros (Smith et al., 1999). E-/N-MORB, enriched and normal mid ocean ridge basalts, LC: lower crust, OIB: oceanic island basalts, PM: primitive mantle, UC: upper crust. (E-N MORB, OIB, PM values are from Sun & McDonough, 1989; LC, UC values are from Rudnick & Gao, 2003)

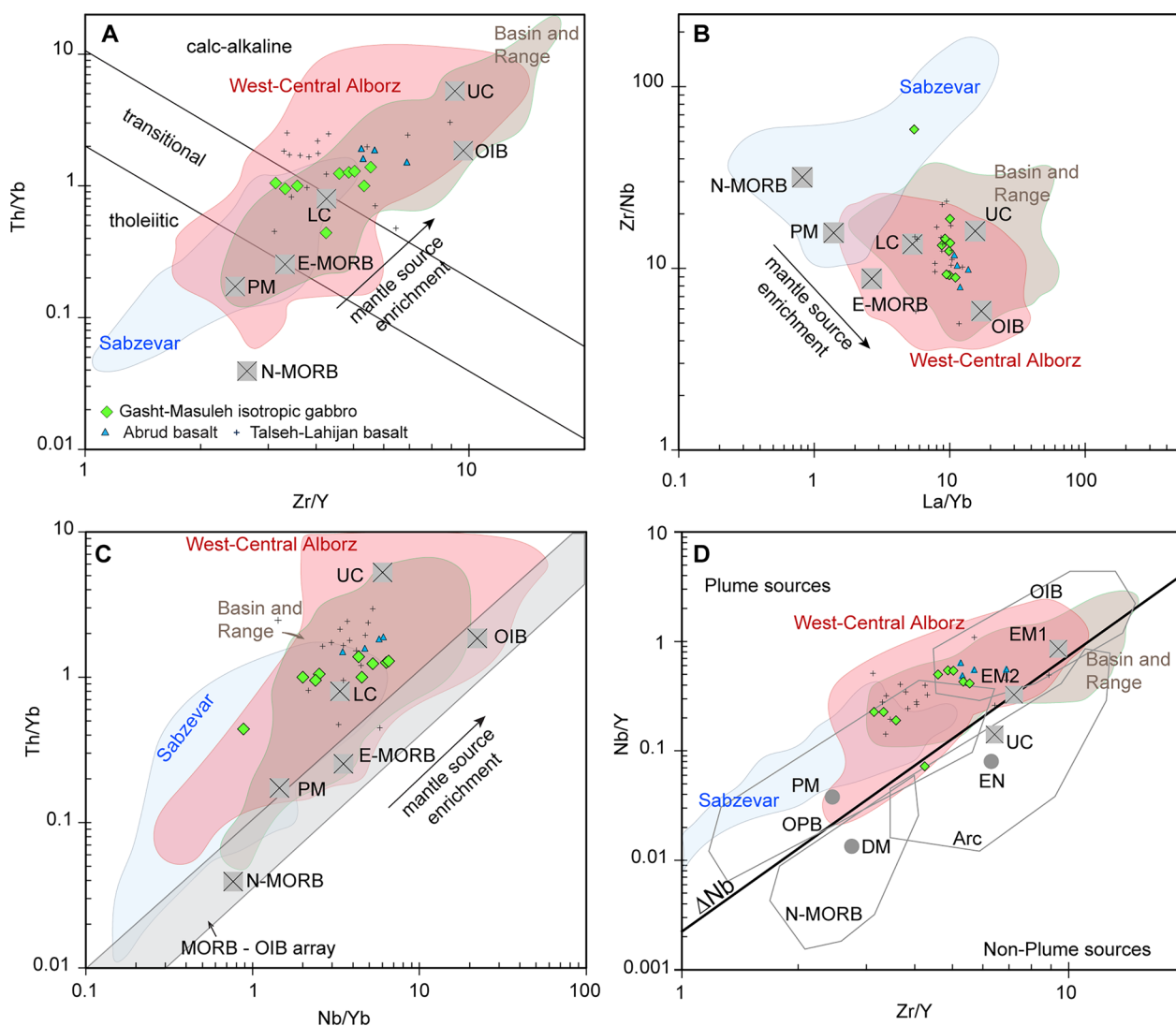


Fig. 9 A Zr/Y vs. Th/Yb (Ross & Bédard, 2009), B La/Yb vs. Zr/Nb, C Nb/Yb vs. Th/Yb (Pearce, 2008), D Zr/Y vs. Nb/Y (Condie, 2005) diagrams. In A, B and C the values of the end-members N- and E-MORB, OIB and PM are from Sun and McDonough, (1989), UC and LC are from Rudnick and Gao, (2003). In D the fields and end-member values are according to Condie, (2005) and references therein. DM: depleted mantle; E-/N-MORB: enriched and normal mid ocean ridge basalts, EM1 and EM2: enriched mantle sources, EN: enriched component, LC: lower crust, OIB: oceanic island basalts, OPB: oceanic plateau basalts; UC: upper crust. Data sources, West-Central Alborz: Masuleh gabbro (Khalatbari Jafari et al., 2016), Abrud basalt (Rezaei et al., 2020), Javaherdasht–Javaherhdeh gabbros (Haghnazar et al., 2011; Monsef et al., 2022), South Amlash basic rocks (Salavati, 2008; Salavati et al., 2013), Talash-Lahijan basalt (Monsef et al., 2022), Marzanabad basalt (Dorozi et al., 2016), and Deylaman igneous complex (Akmali et al., 2019), Sabzevar basic rocks: (Ghasemi et al., 2018; Kazemi et al., 2019; Rahmani et al., 2020; Shafaii Moghadam et al., 2014, 2020; Shojaat et al., 2003); Basin and Range: (Hawkesworth et al., 1995; Hooper et al., 1995)

Zr/Nb=58). This ratio indicates slight Zr enrichment of the mantle source compared to N-MORB (Zr/Nb=32, Sun & McDonough, 1989), although variations in Zr/Nb may also reflect the heterogeneity of the magma source (White & Duncan, 1996) (Fig. 9B). Continental crust is characterised by enrichment in La rather than Nb (Rudnick & Gao, 2003) and, apart from contributions by lithospheric and asthenospheric mantle, low Nb/La suggest contributions by a crustal contaminant during evolution

of the magma. The LREE/HREE (La/Yb) ratios (5 to 13) are within the range of the lower crust to upper crust compositions (5 and 16) of Rudnick and Gao, (2003), implying crustal contamination of the magma (Fig. 9B) or contributions by slab-derived fluids (see below, Fig. 12). The gabbros plot above the MORB-OIB array of Pearce, (2008) (Fig. 9C), indicating some degree of crustal contamination as well as Th/Nb ratios (>0.15) indicate contributions of continental crust to the magma (Shervais,

2022). Compared to primitive mantle, the samples are enriched in Th and Nb and in this respect, have compositions between the lower and upper crust of Rudnick and Gao, (2003). Enrichment of their mantle source is shown in the Zr/Y vs. Nb/Y diagram of Condie, (2005), the samples scatter in the Oceanic Plateau Basalts and OIB fields (Fig. 9D), and have higher Nb/Y ratios than arc-related magmatic rocks. They, thereby, plot above the ΔNb line of Fitton et al., (1997) which points an enriched component contribution (EN) to the magma. The enriched component may either be continental crust, or subcontinental lithospheric mantle that may have inherited a geochemical signature of older subduction processes (Condie, 2005).

Taking La/Yb as a proxy for the degree of melting, the high La/Yb indicate low degrees of melting. Non-modal melting curves calculated for garnet-bearing and spinel lherzolite mantle sources of depleted and primitive composition are shown on the primitive mantle normalised $(La/Yb)_N$ vs. $(Dy/Yb)_N$ plot (Fig. 10). This diagram utilises the fractionation of the middle (Dy) from the heavy (Yb) REE during melting in the garnet peridotite stability field, whereas melting in the spinel-facies produces little change in Dy/Yb ratios (Thirlwall et al., 1994). The Gasht-Masuleh gabbros, Abrud and Talesh-Lahijan basalts plot

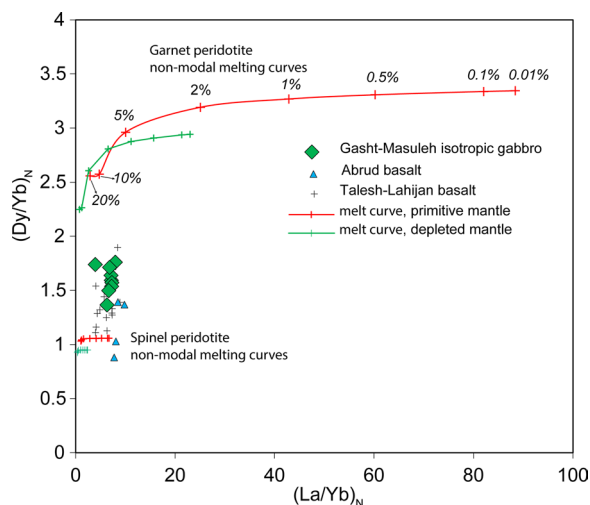


Fig. 10 $(La/Yb)_N$ vs. $(Dy/Yb)_N$ diagram for the Gasht-Masuleh gabbros and mid-Cretaceous basalts (Abrud and Talesh-Lahijan areas). The partial melting curves were calculated using the non-modal aggregated fractional melting model $C_L = (C_0/F) (1 - (1 - PF/D_0)^{1/P})$ of Shaw, (1970). The numbers in italics on the model melting curves indicate degree of melting in percent. The modal mineralogies and mineral/melt partition coefficients are from McKenzie and O’Nions (1991a, 1991b) and the melt proportions are from Thirlwall et al., (1994). The primitive and depleted mantle source compositions are from Hofmann (1988). Primitive Mantle normalisation values for La, Dy and Yb are from Sun and McDonough, (1989)

close to the spinel lherzolite melting curves indicating that mid-Cretaceous gabbros and the basalts in the western Alborz Mountains originate from relatively shallow mantle. This is supported by the relatively flat HREE patterns of the Gasht-Masuleh gabbros that do not indicate the presence of garnet in their source ($(Dy/Yb)_N = 1.4 - 1.8$; Fig. 10).

Comparing published data for basic rocks from the western, central and eastern Alborz (Fig. 9A–E, references for the published data are given in the figure caption), basic rocks in the west and central Alborz and the Gasht-Masuleh gabbros have very similar compositions, whereas those of basic rocks in the east Alborz (Sabzevar area) differ (Additional file 11 shows the location of compared basic rocks). Those in the West Alborz were generated from a mantle source that was more enriched compared to those in the Sabzevar region. Figure 9 shows that basic rocks in the West-Central Alborz were formed in an OIB-like/arc-like tectonic setting, while those in the East Alborz were mostly formed in a MORB setting. As mentioned above, the evolution of the Gasht-Masuleh gabbros magma involved contamination the crustal material. In almost all comparative diagrams, the compositions of the Gasht-Masuleh gabbros and the West-Central Alborz basic rocks overlap with calc-alkaline rocks in the Basin and Range (USA) area (Hawkesworth et al., 1995; Hooper et al., 1995) and in the Eastern Pontides (Turkey) and the Lesser Caucasus (Armenia; Monsef et al., 2022 and references therein) that formed in an extensional tectonic setting.

7.3 Mineral compositions

In the Mg# vs. Al_2O_3 diagram (DeBari & Coleman, 1989) the orthopyroxene does not plot on the Al_2O_3 enrichment trend but along a low pressure differentiation trend due to their relatively low Al_2O_3 contents. This points to crystallisation of the magma under low pressure conditions in a shallow magma chamber at upper crustal levels (Fig. 11A). We have found no petrographic evidence, such as plagioclase crystallisation before olivine, which might have supported shallow levels of crystallisation. Orthopyroxene Al_2O_3 contents range from 0.1 to 1.2 wt.%. The low Al_2O_3 contents of the orthopyroxenes (< 0.6 apfu) are an indicator for low pressures of crystallization. Using Emslie et al. (1994), we calculate very low pressures (ca. 0.23 kbar) that should probably not be taken literally as medium-grained, doleritic textures should be expected, but as an indication for crystallization at shallow crustal levels. Rezaei et al., (2019) point out that the Al_2O_3 , Na_2O and Cr_2O_3 contents of orthopyroxene and clinopyroxene are low, indicating crystallisation at low pressure at upper crustal levels. They obtained temperatures in the range 800–900 °C, using pyroxene thermometry (Köhler

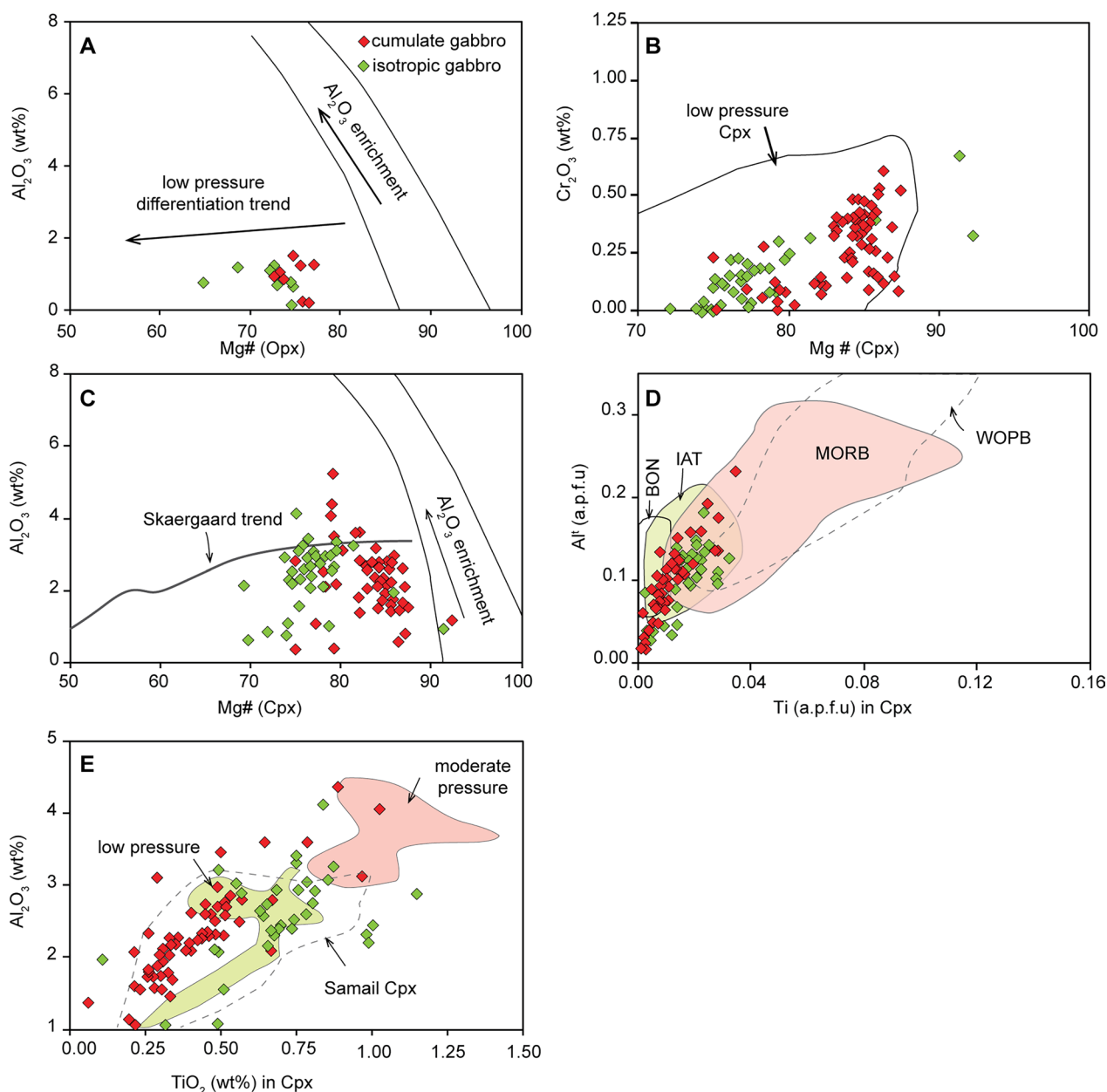


Fig. 11 Mineral composition co-variation diagrams, **A** Orthopyroxene Mg# vs. Al₂O₃ diagram of DeBari and Coleman, (1989). **B** Clinopyroxene Mg# vs. Cr₂O₃ low pressure field from Elthon, (1987). **C** Clinopyroxene Mg# vs. Al₂O₃ diagram of DeBari and Coleman, (1989). **D** Clinopyroxene Ti vs. Al (a.p.f.u) tectonic setting diagram of Beccaluva et al., (1989). **E** Clinopyroxene TiO₂ vs. Al₂O₃ diagram modified by Parlak et al., (2020) with the low and moderate pressure fields after Elthon, (1987), the field of Samail ophiolite clinopyroxenes is from Pallister and Hopson, (1981). BON: boninites, IAT: island-arc tholeiites, MORB: mid-ocean ridge basalts, WOPB: within oceanic plate basalts

& Brey, 1990; Nimis & Taylor, 2000), that are unusually low for mafic melts and do not reflect crystallisation temperatures.

Clinopyroxene Mg# and Cr₂O₃ show a positive correlation for both isotropic and cumulate samples. Clinopyroxene from isotropic gabbros plot mainly in the field of low pressure clinopyroxenes derived from 1 atm

experimental studies of N-MOR basalts (Elthon, 1987) (Fig. 11B). Al₂O₃ content of clinopyroxenes in both cumulate and isotropic samples are low (≤ 5.2 wt%) and do not correlate with Mg#. In the Mg# vs. Al₂O₃ diagram (DeBari & Coleman, 1989) (Fig. 11C) most plot below the low pressure Skaergaard trend. TiO₂ contents of clinopyroxenes of cumulate samples are lower (≤ 1.04 wt%) than

those of isotropic samples (≤ 1.63 wt%). Clinopyroxenes of the Zudel intrusion have moderately high TiO_2 contents (≤ 1.04 wt%), which reflects the higher TiO_2 whole rock abundances of the Zudel samples. The, on average, low Ti contents of clinopyroxenes from both cumulate and isotropic samples from all three intrusions (≤ 0.05 p.f.u) point to Ti depletion of the magma source(s) (Pearce & Norry, 1979).

The TiO_2 and Al_2O_3 contents of the clinopyroxenes plot in the overlapping fields for arc and mid-ocean ridge gabbros (Beccaluva et al., 1989) (Fig. 11D). In the TiO_2 vs. Al_2O_3 diagram for clinopyroxenes from isotropic and cumulate gabbros (Parlak et al., 2020), the clinopyroxenes mainly cluster in the low pressure field with some analyses plotting in the moderate pressure field and beyond (Fig. 11E). The relatively low TiO_2 and Al_2O_3 and high SiO_2 of the analysed clinopyroxenes tend to indicate a calc-alkaline nature for the magma, as clinopyroxene in mid-ocean ridge basalts generally are higher, and those in arc-related basalts lower Ti contents (LeBas, 1962).

7.4 Zircon and phlogopite ages

The 99.5 ± 0.6 Ma and 99.4 ± 0.6 Ma U–Pb zircon Concordia ages for the Zudel leucogabbro and Gilvanderud isotropic gabbro overlap within 2σ error and are interpreted as crystallisation ages of the magmas that must have intruded in the mid-Cretaceous around the (Albian-)Cenomanian boundary. The $^{40}\text{Ar}/^{39}\text{Ar}$ phlogopite step-heating ages for the three intrusions fall in the narrow range ca. 97–98 Ma and are 1 to 2 Ma younger than the U–Pb zircon ages. The younger phlogopite ages agree with the petrographic observations that it is the last phase to crystallise. We consider that the three intrusions crystallised and cooled coevally.

7.5 Comparison with other Cretaceous mafic magmatic rock in the Alborz Mountains

Annells, (1975) reported a 1.5 km thick sequence of Cretaceous (Aptian-Albian) intermediate to mafic lavas in the Qazvin area NW of Tehran (Additional file 11) but presented no geochemical data. Furthermore, basic and plagiogranite dykes in the Sabzevar–Torbat-e-Heidariye area indicate the opening of back-arc basins in NE Iran as a response to an extensional tectonic regime in the Late Cretaceous (ca. 100–110 Ma K–Ar whole rock ages, Delaloye et al., 1981; 91–99 Ma U–Pb zircon age, Shafaii Moghadam et al., 2020). The Chalus Formation exposed in the Marzanabad, Abbasabad and Kojur areas north of Tehran (Additional file 11) comprises several phases of mafic volcanic rocks, such as Barremian alkaline olivine basalts and Turonian high-alumina basalts (Cartier, 1971; Wensink & Varekamp, 1980). These erupted in a shallow marine basin mainly

filled with limestones (Allen et al., 2003) that overlie the Jurassic Shemshak Group with an angular unconformity and are overlain by Aptian-Cenomanian limestones of the Tizkuh Formation (Ansari, 2013; Ansari et al., 2011; Cartier, 1971). Whole rock geochemistry of the olivine basaltic andesites to olivine andesitic basalts of the Kojur and basanites of the Abbasabad volcanic fields indicate that the mantle-derived primary magma were alkaline and originated from a garnet bearing lherzolite source (Ansari, 2013; Ansari et al., 2011). This, and the fact that they erupted onto continental crust points to an intra-continental setting of the Chalus Formation magmatism, e.g. the central Alborz crust (Ansari, 2013; Ansari et al., 2011). Guest et al., (2006 and references therein), reported a 97.4 ± 1.8 Ma ion-probe $^{206}\text{Pb}/^{238}\text{U}$ zircon age for the diorite phase and a 96.9 ± 2.4 Ma age for the (rapakivi) granite phase of the composite Nusha Pluton 150 km to the ESE of the Gasht-Masuleh area. These zircon ages overlap with ca. 97–100 Ma $^{40}\text{Ar}/^{39}\text{Ar}$ phlogopite and U–Pb zircon ages for the Gasht-Masuleh gabbros (this study). This indicates that (Albian-)Cenomanian plutonic activity was not local but occurred over large areas, possibly constituting a long-lasting and widespread mafic volcanoplutonic stage in the Alborz Mountains.

120 km to the east of the Gasht-Masuleh area on the Caspian Sea coast, basic volcanic rocks, small gabbro intrusions and ultramafic cumulates of suspected Cretaceous age occur south of Amlash (Annells, 1975). The gabbros and cumulates have a mantle source that was modified by subduction (Salavati et al., 2013). In contrast, the basalts are alkaline and have an OIB-like mantle source (Salavati, 2008). In the Javaherdasht area 20 km SE of Amlash, isotropic and layered gabbros intrude Jurassic clastic sediments and limestone of the Javaherdeh Formation. The isotropic gabbros have high Na_2O , K_2O , TiO_2 and FeO^t contents compared to the layered gabbros and were probably derived from MORB-like spinel-bearing mantle source(s) and show trace element evidence for contamination with crustal material (Haghnazar et al., 2011). The layered gabbros have high Mg# and high Ni, Cr and Co abundances, both types may have formed in a continental rift setting (Haghnazar et al., 2011). Basalts and gabbros in the Javaherdasht, the Gasht-Masuleh and the Talesh Mountains areas formed in an extensional setting but show an arc geochemical signature that is the result of contamination by crustal components (Haghnazar et al., 2011; Monsef et al., 2022; Rezaei et al., 2019, 2020). Cretaceous magmatic rocks in the Deylaman area (Additional file 11) comprise pillow and sheet lavas, trachytes, alkali rhyolites and olivine gabbro and monzodiorite intrusions with sub-alkaline to alkaline signatures (Akmali et al., 2019).

Comparison of the gabbros in the Gasht-Masuleh area with published data of other Cretaceous mafic magmatic rocks in the Alborz Mountains shows that more than half have elevated Ba/La (i.e. higher than MORB) at relatively low Th/Yb ratios (Fig. 12; Woodhead et al., 2001). This may be attributed to the effects of fluids derived from a previously subducted oceanic slab (Arculus & Powell, 1986; Woodhead et al., 2001), possibly of the Palaeo-Tethys Ocean because most magmatic activities related to Neo-Tethys subduction are concentrated in the Sanandaj-Sirjan Zone far to the south of the Alborz Mountains (Hassanzadeh & Wernicke, 2016). The volcanic rocks in the Chalus area form an exception, trending to high Th/Yb at low Ba/La ratios reflecting mixing of mantle source material with magma derived from subducted sediments (Ansari, 2013; Ansari et al., 2011).

7.6 Tectonic setting

Neo-Tethys oceanic crust subduction beneath the Central Iranian Platform initiated in the Late Triassic and intensified during the Jurassic until the formation of the Cretaceous Sanandaj-Sirjan Arc (Hassanzadeh & Wernicke, 2016 and references therein). Arc-related gabbros near Chaldoran (Rezaei Bargoshadi et al., 2020), acidic to intermediate magmatic rocks near Khoy (112–96 Ma U–Pb zircon ages; Lechmann et al., 2018), diorites and gabbros near Naqadeh (~97 Ma U–Pb zircon age; Mazhari et al., 2011) and near Urmia (99–100 Ma biotite K–Ar, Ghalamghash et al., 2009) argue for arc-related magmatism.

Cretaceous magmatism related to Neo-Tethys subduction is widespread in the Zagros Belt in NE Iraq, where arc related acidic to basic magmatic rocks occur at Kata-Rash (~108 Ma zircon age), basic to intermediate volcanic rocks at Hasanbagh (~106–92 Ma magmatic hornblende $^{40}\text{Ar}/^{39}\text{Ar}$ step-heating ages; Ali et al., 2013, 2016), and oceanic arc-related volcanic and plutonic rocks at Pushtashan (~96 Ma U–Pb zircon age; Ismail et al., 2017). In central Turkey, arc related magmatic rocks formed during Neo-Tethys subduction have Late Cretaceous ages (~92 Ma, U–Pb zircon ages for gabbros and granites; e.g. Temizel et al., 2022; Monsef et al., 2022 and references therein). Middle Jurassic to Late Cretaceous alkaline and calc-alkaline volcanic rocks in the Pontides and Lesser Caucasus have been interpreted as arc related magmatic rocks that formed above the north dipping Neo-Tethys subduction zone (~170–83 Ma; summarised in Hässig et al., 2015 and references therein).

In the Alborz Mountains, tectonic activity was limited in the Cretaceous. Sedimentation was of a quiet nature with low sedimentation rates of predominant shallow marine reef carbonates and marls (Clark et al., 1975; Saidi et al., 1997) and subduction was certainly not taking

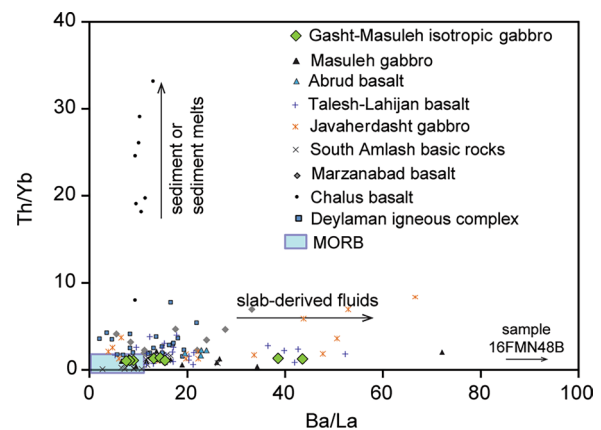


Fig. 12 Comparison of the Gasht-Masuleh gabbros and other Cretaceous igneous rocks of the Alborz Mountains. Ba/La vs. Th/Yb diagram of Woodhead et al., (2001). Data sources: Abrud basalt (Rezaei et al., 2020), Talash-Lahijan basalt (Monsef et al., 2022), Masuleh gabbro (Khalatbari Jafari et al., 2016), Javaherdasht gabbro (Haghnazar et al., 2011; Monsef et al., 2022), South Amlash basic rocks (Salavati, 2008; Salavati et al., 2013), Marzanabad basalt (Doroozi et al., 2016), Chalus basalt (Ansari, 2013) and Deylaman igneous complex (Akmali et al., 2019)

place in this area. Guest et al. (2006) tentatively suggested that the Cretaceous magmatic activity might be related to subduction of the Neo-Tethys Ocean and arc formation in the Zagros Belt at least 380 km to the SW, implying that a very wide area was affected by this subduction system. Thus, the mantle derived magmatism in the Alborz Mountains may be due to extension causing mantle melting, both triggered by far-field effects of the Neo-Tethys subduction zone. A similar setting was proposed for the Permo-Carboniferous mafic magmatism in the foreland of the Variscan Orogen in Europe (e.g. Timmerman, 2004).

Geochemical data for the Gasht-Masuleh gabbros such as Ti, Nb and Ta negative anomalies, low Nb/Th and elevated and variable Ba/La ratios, indicate that their magma was derived from a mantle source marked an arc signature. In general, mantle metasomatism appears to be mainly the result of slab-derived fluids, except for the alkaline basalts of the Chalus Formation that show evidence for contributions from subducted sediments (Fig. 12). The Cenomanian plate tectonic reconstruction of Barrier et al., (2018) (Fig. 13) illustrates that north-dipping Neo-Tethys subduction occurred in the future Zagros Belt and that in the northeastern, over-riding plate, extension-related magmatism took place in the Alborz Mountains. Here, magmatism occurred in a shallow marine environment and was associated with faulting that probably facilitated the magma ascent such as that of the Gasht-Masuleh gabbros. As there is no evidence for Jurassic-Cretaceous subduction in the Alborz

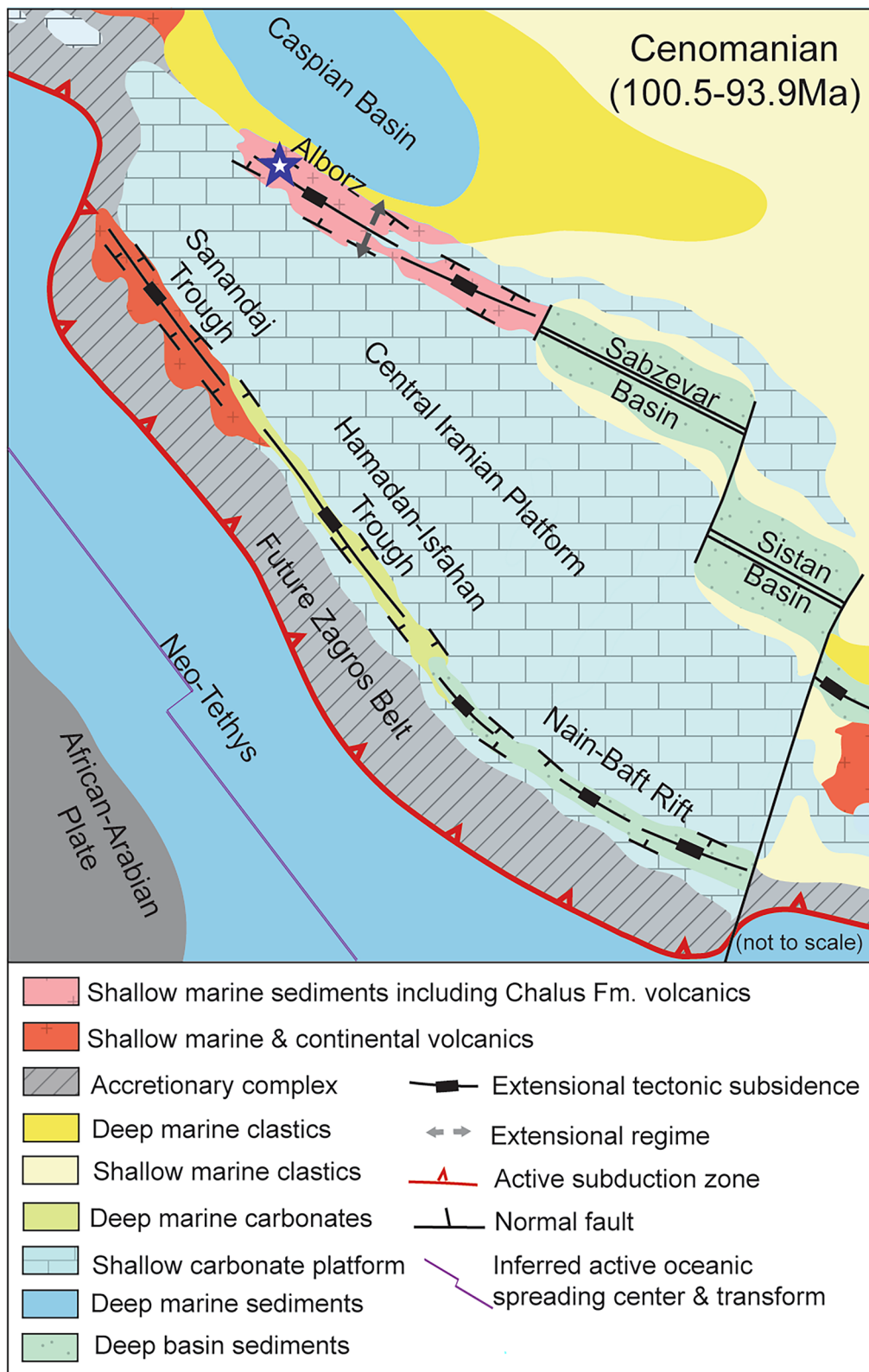


Fig. 13 Palaeotectonic reconstruction of Iran (modified from Barrier et al., 2018) showing the approximate position of the study area (star symbol) in Cenomanian in relation to the zone of active subduction of the Neo-Tethys slab beneath the Central Iranian Platform, causing basin formation and extension-related magmatism in the Alborz Mountains

Mountains, these signatures must have been inherited from an older event, probably subduction of the Palaeo-Tethys Ocean in the Carboniferous and its closure in the Triassic (Stampfli & Borel, 2002). The Palaeo-Tethys suture is assumed to lie to the north of the Alborz Mountains (e.g. Omrani et al., 2013; Stampfli & Kozur, 2006). Local normal faulting and the generation of small volumes of magmatic rocks in the Alborz Mountains in the Cretaceous were probably the response to extension and the far field tectonic effects of slab roll-back and back-arc opening due to the north dipping Neo-Tethys subduction zone in central Iran (Agard et al., 2011). The short-lived, local, relatively small volume and often mafic mid-Cretaceous magmatism in the Gasht-Masuleh area may be linked to such short-lived extension stages that caused passive mantle upwelling and low degree mantle decompression melting (Fig. 14). Relatively rapid ascent of the mantle-derived magma probably took place along deep-seated fault zones. These may have been newly formed normal faults or reactivated old faults (including thrusts and strike-slip faults) inherited from closure of the Palaeo-Tethys Ocean in the Late Triassic.

8 Conclusions

Dating of magmatic zircon and phlogopite shows that in the Gasht-Masuleh area, intrusion and crystallisation of mantle derived mafic magma occurred at ca. 100 Ma during the mid-Cretaceous times. The magma shows

normal gabbroic fractionation ($Ol \rightarrow Ol + Cpx + magnetite-ilmenite \pm Opx \rightarrow Pl + magnetite-ilmenite$). The relatively low Mg# of the olivines indicates that the magma was fractionated before intrusion emplacement. Crystallisation occurred at relatively high crustal levels indicated by the low Al contents of clino- and orthopyroxenes, defining a low pressure differentiation trend. Clinopyroxene compositions point to a low Ti, calc-alkaline magma, which is supported by the transitional to calc-alkaline whole rock major and trace element compositions.

Gasht-Masuleh gabbros are slightly enriched in LREE resulting in sloping REE patterns that generally lack Eu anomalies. Although there is no evidence for active subduction and arc magmatism in Alborz in the Cretaceous, Nb and Ta negative anomalies in multi-element diagrams point to the presence of an arc-related component, as do the variable Ti abundances which, however, may also be due to the fractionation of magnetite-ilmenite exsolution. Overall, the trace element signature points to the presence of an arc-related component inherited from the mantle source, with possible contamination by crustal components.

In summary, trace element compositions indicate that the gabbros in the Gasht-Masuleh area (and many other Cretaceous mafic magmatic rocks in the Alborz Mountains) were generated by partial melting of a metasomatized mantle source. The most likely explanation is that mantle metasomatism occurred during subduction of the

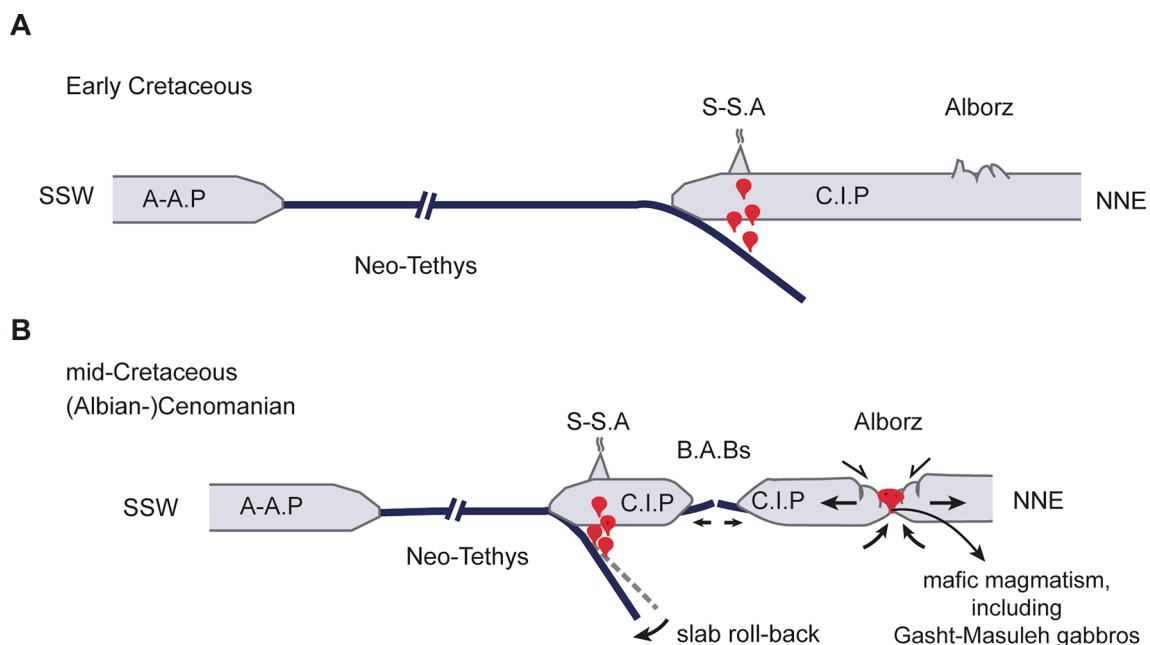


Fig. 14 A–B Plate tectonic model illustrating Cretaceous extension and mafic magmatism in the Alborz Mountains (including the small Gasht-Masuleh gabbro intrusions) due to far-field effects caused by the initiation of Neo-Tethys slab roll-back. Abbreviations: A-A.P (African-Arabian Plate), C.I.P. (Central Iranian Platform), S-S.A (Sanandaj-Sirjan Arc), B.A.B (back-arc basin)

Palaeo-Tethys Ocean in north Iran in Palaeozoic–Triassic times, and that the arc/subduction signature of the gabbros is an inherited feature (e.g. Monsef et al., 2022; Woodhead et al., 2001).

U–Pb zircon and $^{40}\text{Ar}/^{39}\text{Ar}$ phlogopite ages show that the Gasht-Masuleh gabbros intruded in (Albian-)Cenomanian times and cooled rapidly, indicating magma generation, intrusion and cooling at high crustal levels all taking place during a short-lived extensional event. This event was not restricted to the Gasht-Masuleh area but also occurred further to the SSE in the area NW of Tehran (ca. 97 Ma Nusha diorite-granite composite pluton, Guest et al., 2006). In general, the mid-Cretaceous magmatism may reflect extension of the crust caused by slab roll-back initiation of the northward subducting Neo-Tethys Ocean.

Supplementary Information

The online version contains supplementary material available at <https://doi.org/10.1186/s00015-023-00443-2>.

Additional file 1: S1.1 Petrography of the Gasht-Masuleh cumulate gabbros. S1.2. Detailed descriptions of the analytical methods.

Additional file 2: Table S2. XRF, ICP-OES and ICP-MS major oxide, trace and rare earth element concentration of the gabbros from the Gasht-Masuleh area, Alborz Mountains, N Iran. $\text{Mg\#} = 100 \times \text{Mg}/(\text{Mg} + \text{Fe}^{2+})$, $\text{Fe}^{2+} = (\text{FeO} \times 0.89981/71.84)$; Abbreviations: n.d.: not determined; b.d.: below detection limit; UP: Institute of Geosciences, University of Potsdam (Germany); GFZ: GeoForschungsZentrum Potsdam (Germany); Actlabs: Activation Laboratories Ltd. (Ancaster, Canada).

Additional file 3: Table S3. Electron probe micro analyses of olivine from the gabbros from Gasht-Masuleh area, Alborz Mountains, N Iran. $\text{Mg\#} = 100 \times \text{Mg}/(\text{Mg} + \text{Fe}^{2+})$; Fo (forsterite) = $100 \times \text{Mg}/(\text{Mg} + \text{Fe}^{2+} + \text{Mn})$; Fa (fayalite) = $100 \times \text{Fe}^{2+}/(\text{Mg} + \text{Fe}^{2+} + \text{Mn})$; Teph (tephroite) = $100 \times \text{Mn}/(\text{Mg} + \text{Fe}^{2+} + \text{Mn})$.

Additional file 4: Table S4. Electron probe micro analyses of orthopyroxene from the gabbros from Gasht-Masuleh area, Alborz Mountains, N Iran. $\text{Mg\#} = 100 \times \text{Mg}/(\text{Mg} + \text{Fe}^{2+})$; Wo (wollastonite) = $100 \times \text{Ca}/(\text{Mg} + \text{Fe}^{2+} + \text{Ca})$; En (enstatite) = $100 \times \text{Mg}/(\text{Mg} + \text{Fe}^{2+} + \text{Ca})$; Fs (ferrosilite) = $100 \times \text{Fe}^{2+}/(\text{Mg} + \text{Fe}^{2+} + \text{Ca})$. **Figure S4.** Nomenclature of orthopyroxene of the Gasht-Masuleh gabbros (Morimoto, 1988).

Additional file 5: Table S5.1 and S5.2 Electron probe micro analyses of clinopyroxene from the gabbros from Gasht-Masuleh area, Alborz Mountains, N Iran, carried out at University of Potsdam (S5.1) and the GFZ (S5.2). $\text{Mg\#} = 100 \times \text{Mg}/(\text{Mg} + \text{Fe}^{2+})$; Wo (wollastonite) = $100 \times \text{Ca}/(\text{Mg} + \text{Fe}^{2+} + \text{Ca})$; En (enstatite) = $100 \times \text{Mg}/(\text{Mg} + \text{Fe}^{2+} + \text{Ca})$; Fs (ferrosilite) = $100 \times \text{Fe}^{2+}/(\text{Mg} + \text{Fe}^{2+} + \text{Ca})$. **Figure S5.** Nomenclature of clinopyroxene of the Gasht-Masuleh gabbros (Morimoto, 1988).

Additional file 6: Tables S6.1 and S6.2 Electron probe micro analyses of plagioclase from the gabbros from Gasht-Masuleh area, Alborz Mountains, N Iran, carried out at University of Potsdam (S6.1) and the GFZ (S6.2). Ab (albite) = $100 \times \text{Na}/(\text{Ca} + \text{Na} + \text{K})$; An (anorthite) = $100 \times \text{Ca}/(\text{Ca} + \text{Na} + \text{K})$; Or (orthoclase) = $100 \times \text{K}/(\text{Ca} + \text{Na} + \text{K})$. **Figure S6.** Nomenclature of plagioclase of the Gasht-Masuleh gabbros (Smith, 1974)

Additional file 7: Tables S7.1 and S7.2 Electron probe micro analyses of phlogopite from the gabbros from Gasht-Masuleh area, Alborz Mountains, N Iran, carried out at University of Potsdam (S7.1) and the GFZ (S7.2). $\text{Mg\#} = 100 \times \text{Mg}/(\text{Mg} + \text{Fe})$. **Figure S7.** Nomenclature of phlogopite of the Gasht-Masuleh gabbros (Deer et al., 1992).

Additional file 8: S8. Summary petrography of the dated samples 15FMN06 (leucocratic gabbro), GH 16-77 (isotropic gabbro), and

16FMN20A, 16FMN45A and 15FMN05A (all clinopyroxene cumulates). **Figure S8.1.** Photomicrograph of phlogopite in sample 16FMN20A in plane polarized light. Abbreviations: Cpx = clinopyroxene, Phl = phlogopite, Pl = plagioclase. **Figure S8.2.** Photomicrograph of phlogopite in sample 16FMN45A in plane polarized light. Abbreviations: Chl = chlorite, Cpx = clinopyroxene, Phl = phlogopite, Ol = olivine, Pl = plagioclase. **Figure S8.3.** Photomicrograph of phlogopite in sample 15FMN05A in plane polarized light. Abbreviations: Cpx = clinopyroxene, Ol = olivine, Phl = phlogopite, Pl = plagioclase.

Additional file 9: Table S9.1. LA-ICP-MS U–Th–Pb isotope data of zircons from the Zudel and Gilvanderud gabbros in the Gasht-Masuleh area, Alborz Mountains, N Iran. Analyses were carried out at the Institute of Geology of the Czech Academy of Sciences, Prague, Czech Republic. $\text{Disc.} = (1 - ((^{206}\text{Pb}/^{238}\text{U}) / (^{207}\text{Pb}/^{235}\text{U}))) \times 100$ for zircons younger than 1 Ga. $^{206}\text{Pb}/^{238}\text{U}$ final ages in bold font were used to label spot ages and those in italics to calculate pooled ages. **Table S9.2.** LA-ICP-MS U–(Th–)Pb analytical data reporting sheet (template according to Horstwood et al., 2016). **Figure S9.1.** Ranked order plots of $^{206}\text{Pb}/^{238}\text{U}$ ages of the zircons from the Gasht-Masuleh gabbros. **Figure S9.2.** Concordia diagrams of all the ages obtained from the analyzed points of the zircons from the Gasht-Masuleh gabbros.

Additional file 10: Table S10. $^{40}\text{Ar}/^{39}\text{Ar}$ incremental step-heating data for phlogopites from the Zudel, Gilvanderud and Chapul cumulate gabbros in the Gasht-Masuleh area, Alborz Mountains, N Iran. Analyses were carried out at the Argon Geochronology Laboratory of the Institute of Geosciences at the University of Potsdam. Gas fractions in bold font were used for plateau (16FMN20A, 16FMN45A) or forced plateau age calculations (15FMN05A). Analytical uncertainties are presented at 1- σ level. t.f. = total fusion. Irradiation parameters are included at the bottom of the table.

Additional file 11: Figure S11. Simplified 1:1000,000 geological map of N Iran (Sahandi & Soheili, 2014), showing the location of basic rocks that are compositionally compared to the Gasht-Masuleh gabbros.

Acknowledgements

The first author gratefully acknowledges funding for sabbatical leave from the Ministry of Science, Research and Technology of Iran. L.R. also thanks Prof. Dr. Max Wilke for his support during her stay at the Institute of Geosciences of the University of Potsdam. The University of Tabriz is thanked for logistical support during field work. Christine Fischer is thanked for thin section preparation and Antje Musiol for ICP-OES analyses. Ghasem Heidarzadeh is thanked for his donation of gabbro sample GH16-77 from the Gasht-Masuleh area. L.R. thanks Mahya Rezaei Bargoshadi and Zohre Salimi for their company during field work. Discussion with Prof. Roland Oberhänsli is gratefully acknowledged. The authors are grateful for the comments and suggestions of two anonymous journal reviewers that significantly improved the manuscript, and for the editorial handling by Dr. Paola Manzotti and Dr. Daniel Marty.

Author contributions

LR: carried out field work, sample preparation, and the analytical part of the research, and wrote the scientific text, MJT: supervised first author during the data collecting and writing, edited the scientific text, MM: supervised the first author during the field work and the writing, edited the scientific text, UA: Edited the scientific text, JS: carried out the LA-ICP-MS U–Pb zircon dating and edited the LA-ICP-MS method section, MS: carried out the $^{40}\text{Ar}/^{39}\text{Ar}$ step heating dating along with first author and edited the $^{40}\text{Ar}/^{39}\text{Ar}$ step heating method section, CG: supervised the electron probe micro analysis of the minerals and edited the EPMA method section, FDW: carried out the trace element measurement of the selected minerals and edited the EPMA method section, AMS: carried out the ICP-MS measurement of the whole rock samples for selected trace elements and edited the ICP-MS method section.

Funding

Open Access funding enabled and organized by Projekt DEAL. Funded by the Deutsche Forschungsgemeinschaft (DFG, German Research Foundation)—Projektnummer 491466077. Jiří Sláma was supported by the Academy of Sciences of the Czech Republic institutional support to the Institute of Geology, ASCR, RVO 67985831.

Availability of data and materials

All data generated or analysed during this study are included in this published article [and its supplementary information files].

Declarations**Competing interests**

The authors declare that they have no competing interests.

Author details

¹Institute of Geosciences, University of Potsdam, Karl-Liebknecht-Strasse 24-25, Haus 27, 14476 Potsdam-Golm, Germany. ²Department of Earth Sciences, University of Tabriz, Tabriz 51666, Iran. ³The Department of Earth and Environmental Sciences, University of Central Asia, Khorog 736000, Tajikistan. ⁴Institute of Geology, The Czech Academy of Sciences, 16500 Prague 6, Czech Republic. ⁵Helmholtz-Zentrum Potsdam, GeoForschungsZentrum (GFZ), Telegrafenberg, 14473 Potsdam, Germany.

Received: 26 April 2023 Accepted: 26 August 2023

Published online: 22 September 2023

References

- Agard, P., Omrani, J., Jolivet, L., Whitechurch, H., Vrielynck, B., Spakman, W., Monié, P., Meyer, B., & Wortel, R. (2011). Zagros orogeny: A subduction-dominated process. *Geological Magazine*, 148(5–6), 692–725.
- Akmali, S., Asiabanha, A., & Haghazadeh, S. (2019). Cretaceous magmatic evolution in the Deylaman igneous complex, Alborz zone, Iran: Change from extensional to compressional regime. *Geological Quarterly*, 63, 757–770. <https://doi.org/10.7306/gq.1500>
- Ali, S. A., Buckman, S., Aswad, K. J., Jones, B. G., Ismail, S. A., & Nutman, A. P. (2013). The tectonic evolution of a Neo-Tethyan (Eocene–Oligocene) island-arc (Walash and Naopurdan groups) in the Kurdistan region of the Northeast Iraqi Zagros Suture Zone. *Island Arc*, 22(1), 104–125.
- Ali, S. A., Ismail, S. A., Nutman, A. P., Bennett, V. C., Jones, B. G., & Buckman, S. (2016). The intra-oceanic Cretaceous (~ 108 Ma) Kata-Rash arc fragment in the Kurdistan segment of Iraqi Zagros suture zone: Implications for Neotethys evolution and closure. *Lithos*, 260, 154–163.
- Allen, M. B., Ghassemi, M. R., Shahrabi, M., & Qorashi, M. (2003). Accommodation of late Cenozoic oblique shortening in the Alborz range, northern Iran. *Journal of Structural Geology*, 25(5), 659–672.
- Anells, R.N. (1975). Explanatory text of the Qazvin and Rasht quadrangles map. Geological survey, Iran, Tehran, 3.
- Ansari, M. R. (2013). Geochemistry of Mid Cretaceous Alkaline Volcanic Rocks, member of Chalooos formation, Abbas Abad Volcanic Field, Central Alborz Mountains North of Iran. *Life Science Journal*, 10(7s), 874–883.
- Ansari, M. R., Abedini Vossoughi, M., Darvishzadeh, A., Sheikhzakariaee, S. J., & Mirzaee Beni, Z. H. (2011). Geochemical constrain on the early cretaceous, OIB-type alkaline volcanic rocks in Kojor volcanic field, central Alborz Mountain, north of Iran. *Australian Journal of Basic and Applied Sciences*, 5, 913–925.
- Arculus, R. J., & Powell, R. (1986). Source component mixing in the regions of arc magma generation. *Journal of Geophysical Research: Solid Earth*, 91(B6), 5913–5926.
- Asiabanha, A., & Foden, J. (2012). Post-collisional transition from an extensional volcano-sedimentary basin to a continental arc in the Alborz Ranges, N-Iran. *Lithos*, 148, 98–111.
- Barrier, E., Vrielynck, B., Brouillet, J.F., & Brunet, M.F. (2018). Paleotectonic reconstruction of the central tethyan realm, paleoreconstruction: 98 Ma, eurasia fixed, cenomanian (100.5–93.9 Ma). Commission for the geological map of the world (CGMW/CCGM), Paris, France., Map 9, (Scale: 1/15000000).
- Beccaluva, L., Macciotta, G., Piccardo, G. B., & Zeda, O. (1989). Clinopyroxene composition of ophiolite basalts as petrogenetic indicator. *Chemical Geology*, 77(3–4), 165–182.
- Buddington, A. F., & Lindsley, D. H. (1964). Iron-titanium oxide minerals and synthetic equivalents. *Journal of Petrology*, 5(2), 310–357.
- Cartier, E. G. (1971). *Die Geologie des unteren Chalus Tals Zentral-Alborz/Iran* (p. 164). Technischen Hochschule und der Universität Zürich.
- Chu, Y., Allen, M. B., Wan, B., Chen, L., Lin, W., Talebian, M., Wu, L., Xin, G., & Feng, Z. (2021). Tectonic exhumation across the Talesh-Alborz Belt, Iran, and its implication to the Arabia-Eurasia convergence. *Earth-Science Reviews*, 221, 103776.
- Clark, G.C., Davies, R.G., Hamzepour, B., & Jones, C.R. (1975). Explanatory text of the Bandar-e-Pahlavi Quadrangle map. Geological survey, Iran, Tehran.
- Condie, K. C. (2003). Incompatible element ratios in oceanic basalts and komatiites: Tracking deep mantle sources and continental growth rates with time. *Geochemistry Geophysics Geosystems*, 4(1), 1–28.
- Condie, K. C. (2005). High field strength element ratios in Archean basalts: A window to evolving sources of mantle plumes? *Lithos*, 79(3–4), 491–504.
- Davies, R.G., Jones, C.R., Hamzepour, B., & Clark, G.C. (1972). Geology of the Masuleh Sheet, NW Iran, scale, 1:100000. Geological survey, Iran, Tehran, Report, 24.
- DeBari, S. M., & Coleman, R. G. (1989). Examination of the deep levels of an island arc: Evidence from the Tonsina ultramafic-mafic assemblage, Tonsina, Alaska. *Journal of Geophysical Research Solid Earth*, 94(B4), 4373–4391.
- Delaloye, M., Jenny, J., & Stampfli, G. (1981). K-Ar dating in the eastern Elburz (Iran). *Tectonophysics*, 79(1–2), T27–T36.
- Doroози, R., Vaccaro, C., Masoudi, F., & Petrini, R. (2016). Cretaceous alkaline volcanism in south Marzanabad, northern central Alborz, Iran: Geochemistry and petrogenesis. *Geoscience Frontiers*, 7(6), 937–951.
- Doroози, R., Vaccaro, C., Masoudi, F., & Petrini, R. (2018). Petrogenesis and mantle source characteristics of Triassic alkaline basaltic rocks of North Kamarbon, Northern Central Alborz Iran. *Solid Earth Sciences*, 3(4), 115–129.
- Elthon, D. (1987). Petrology of gabbroic rocks from the Mid-Cayman Rise spreading center. *Journal of Geophysical Research Solid Earth*, 92(B1), 658–682.
- Emslie, R. F., Hamilton, M. A., & Thériault, R. J. (1994). Petrogenesis of a mid-Proterozoic anorthosite-mangerite-charnockite-granite (AMCG) complex: Isotopic and chemical evidence from the Nain Plutonic Suite. *The Journal of Geology*, 102(5), 539–558.
- Fitton, J. G., Saunders, A. D., Norry, M. J., Hardarson, B. S., & Taylor, R. N. (1997). Thermal and chemical structure of the Iceland plume. *Earth and Planetary Science Letters*, 153(3–4), 197–208.
- Fürsich, F. T., Wilmsen, M., Seyed-Emami, K., Cecca, F., & Majidifard, M. R. (2005). The upper Shemshak formation (Toarcian–Alenian) of the Eastern Alborz (Iran): Biota and palaeoenvironments during a transgressive–regressive cycle. *Facies*, 51, 365–384.
- Fürsich, F. T., Wilmsen, M., Seyed-Emami, K., & Majidifard, M. R. (2009). The Mid-Cimmerian tectonic event (Bajocian) in the Alborz Mountains, Northern Iran: Evidence of the break-up unconformity of the South Caspian Basin. *Geological Society London Special Publications*, 312(1), 189–203.
- Ghalamghash, J., Nédélec, A., Bellon, H., Abedini, M. V., & Bouchez, J. L. (2009). The Urumieh plutonic complex (NW Iran): A record of the geodynamic evolution of the Sanandaj-Sirjan zone during Cretaceous times—Part I: Petrogenesis and K/Ar dating. *Journal of Asian Earth Sciences*, 35(5), 401–415.
- Ghasemi, H., Kazemi, Z., Mousivand, F., & Griffin, W. (2018). Whole-rock geochemistry and mineral chemistry of the late cretaceous dacites in SW Sabzevar: Constrain on their origin and tectonic setting. *Petrology*, 9(3), 79–100.
- Guest, B., Stockli, D. F., Grove, M., Axen, G. J., Lam, P. S., & Hassanzadeh, J. (2006). Thermal histories from the central Alborz Mountains, northern Iran: Implications for the spatial and temporal distribution of deformation in northern Iran. *Geological Society of America Bulletin*, 118(11–12), 1507–1521.
- Haggerty, S. E. (1991). Chapter 5 Oxide Textures—A mini-atlas. In D. H. Lindsley (Ed.), *Oxide minerals: Petrologic and magnetic significance Mineralogical Society of America Reviews in Mineralogy*. Berlin: De Gruyter.
- Haghazadeh, S., Malakotian, S., & Alahyari, K. (2011). Investigation of petrological, mineralogical and geochemical properties of Javaherdasht gabbros (east of Guilan province). *Iranian Journal of Crystallography and Mineralogy*, 18(4), 545–562.
- Hassanzadeh, J., Stockli, D. F., Horton, B. K., Axen, G. J., Stockli, L. D., Grove, M., Schmitt, A. K., & Walker, J. D. (2008). U-Pb zircon geochronology of late Neoproterozoic–Early Cambrian granitoids in Iran: Implications for paleogeography, magmatism, and exhumation history of Iranian basement. *Tectonophysics*, 451(1–4), 71–96.
- Hassanzadeh, J., & Wernicke, B. P. (2016). The Neotethyan Sanandaj-Sirjan zone of Iran as an archetype for passive margin-arc transitions. *Tectonics*, 35(3), 586–621.

- Hässig, M., Rolland, Y., & Sosson, M. (2015). From seafloor spreading to obduction: Jurassic-Cretaceous evolution of the northern branch of the Neotethys in the Northeastern Anatolian and lesser Caucasus regions. *Geological Society London Special Publications*, 428(1), 41–60.
- Hawkesworth, C., Turner, S., Gallagher, K., Hunter, A., Bradshaw, T., & Rogers, N. (1995). Calc-alkaline magmatism, lithospheric thinning and extension in the Basin and Range. *Journal of Geophysical Research: Solid Earth*, 100(B6), 10271–10286.
- Hofmann, A. W. (1988). Chemical differentiation of the Earth: The relationship between mantle, continental crust, and oceanic crust. *Earth and Planetary Science Letters*, 90(3), 297–314.
- Hooper, P. R., Bailey, D. G., & Holder, G. M. (1995). Tertiary calc-alkaline magmatism associated with lithospheric extension in the Pacific Northwest. *Journal of Geophysical Research Solid Earth*, 100(B6), 10303–10319.
- Howie, R. A., Zussman, J., & Deer, W. (1992). *An introduction to the rock-forming minerals* (p. 696). Longman.
- Ismail, S. A., Ali, S. A., Nutman, A. P., Bennett, V. C., & Jones, B. G. (2017). The Pushtashan juvenile suprasubduction zone assemblage of Kurdistan (northeastern Iraq): A Cretaceous (Cenomanian) Neo-Tethys missing link. *Geoscience Frontiers*, 8(5), 1073–1087.
- Kazemi, Z., Ghasemi, H., Tilhac, R., Griffin, W., Moghadam, H. S., O'Reilly, S., & Mousivand, F. (2019). Late Cretaceous subduction-related magmatism on the southern edge of Sabzevar basin, NE Iran. *Journal of the Geological Society*, 176(3), 530–552.
- Khalatbari Jafari, M., Lashani, Z., & Omrani, J. (2016). Petrology of mafic and ultramafic rocks of Masuleh area, Gilan Province. *Researches in Earth Sciences*, 25, 91–108.
- Köhler, T. P., & Brey, G. (1990). Calcium exchange between olivine and clinopyroxene calibrated as a geothermobarometer for natural peridotites from 2 to 60 kb with applications. *Geochimica Et Cosmochimica Acta*, 54(9), 2375–2388.
- Le Bas, M. J. (1962). The role of aluminum in igneous clinopyroxenes with relation to their parentage. *American Journal of Science*, 260(4), 267–288.
- Lechmann, A., Burg, J. P., Ulmer, P., Mohammadi, A., Guillong, M., & Faridi, M. (2018). From Jurassic rifting to Cretaceous subduction in NW Iranian Azerbaijan: Geochronological and geochemical signals from granulites. *Contributions to Mineralogy and Petrology*, 173, 1–16.
- Mazhari, S. A., Amini, S., Ghalamghash, J., & Bea, F. (2011). The origin of mafic rocks in the Naqadeh intrusive complex, Sanandaj-Sirjan Zone NW Iran. *Arabian Journal of Geosciences*, 4(7–8), 1207–1214.
- McKenzie, D. A. N., & O'Nions, R. K. (1991a). Partial melt distributions from inversion of rare earth element concentrations. *Journal of Petrology*, 32(5), 1021–1091.
- McKenzie, D. A. N., & O'Nions, R. K. (1991b). Corrections to 'Partial Melt distributions from Inversion of Rare Earth Element Concentrations'. *Journal of Petrology*, 33(6), 1453.
- Monsef, I., Zhang, Z., Shabaniyan, E., le Roux, P., & Rahgoshay, M. (2022). Tethyan subduction and Cretaceous rift magmatism at the southern margin of Eurasia: Evidence for crustal evolution of the South Caspian Basin. *Earth Science Reviews*, 228, 104012.
- Morimoto, N. (1988). Nomenclature of pyroxenes. *Mineralogy and Petrology*, 39, 55–76.
- Nazari, H., Omrani, J., Shahidi, A., Salamati, R., Mousavi, A. (2004). Geological map of Bandar-e-Anzali sheet, Scale 1:100000. Geological survey, Iran, Tehran.
- Nimis, P., & Taylor, W. R. (2000). Single clinopyroxene thermobarometry for garnet peridotites. Part I. Calibration and testing of a Cr-in-Cpx barometer and an enstatite-in-Cpx thermometer. *Contributions to Mineralogy and Petrology*, 139, 541–554.
- Omrani, H., Moazzen, M., Oberhänsli, R., Tsujimori, T., Bousquet, R., & Moayyed, M. (2013). Metamorphic history of glaucophane-paragonite-zoisite eclogites from the Shanderman area, northern Iran. *Journal of Metamorphic Geology*, 31(8), 791–812.
- Pallister, J. S., & Hopson, C. A. (1981). Samail ophiolite plutonic suite: Field relations, phase variation, cryptic variation and layering, and a model of a spreading ridge magma chamber. *Journal of Geophysical Research Solid Earth*, 86(B4), 2593–2644.
- Parlak, O., Bağcı, U., Rızaoğlu, T., Ionescu, C., Önal, G., Höck, V., & Kozlu, H. (2020). Petrology of ultramafic to mafic cumulate rocks from the Gökşun (Kahramanmaraş) ophiolite, southeast Turkey. *Geoscience Frontiers*, 11, 109–128.
- Pearce, J.A. (1982). Trace element characteristics of lavas from destructive plate boundaries. Orogenic andesites and related rocks, 528–548.
- Pearce, J. A. (2008). Geochemical fingerprinting of oceanic basalts with applications to ophiolite classification and the search for Archean oceanic crust. *Lithos*, 100, 14–48.
- Pearce, J. A., & Norry, M. J. (1979). Petrogenetic implications of Ti, Zr, Y, and Nb variations in volcanic rocks. *Contributions to Mineralogy and Petrology*, 69(1), 33–47.
- Rahmani, F., Mackizadeh, M. A., Noghreyan, M., Marchesi, C., & Garrido, C. J. (2020). Petrology and geochemistry of mafic and ultramafic cumulate rocks from the eastern part of the Sabzevar ophiolite (NE Iran): Implications for their petrogenesis and tectonic setting. *Geoscience Frontiers*, 11(6), 2347–2364.
- Rezaei Bargoshadi, M., Moazzen, M., & Yang, T. N. (2020). Geochemistry of arc-related mantle peridotites and gabbros from the Chaldoran ophiolite NW Iran. *International Geology Review*, 62(13–14), 1724–1750.
- Rezaei, L., Moazzen, M., & Timmerman, M. J. (2019). Magmatic characteristics and crystallisation condition of the Gasht-Masuleh gabbros (North of Iran) based on clinopyroxene and orthopyroxene composition. *Petrology*, 10(3), 131–148.
- Rezaei, L., Moazzen, M., & Timmerman, M. J. (2020). Geochemistry and clinopyroxene mineral chemistry of basalts in the Gasht-Masuleh area, Alborz Mountains. *Iranian Journal of Crystallography and Mineralogy*, 28(3), 623–632.
- Ross, P. S., & Bédard, J. H. (2009). Magmatic affinity of modern and ancient subalkaline volcanic rocks determined from trace-element discriminant diagrams. *Canadian Journal of Earth Sciences*, 46(11), 823–839.
- Rudnick, R., & Gao, S. (2003). Composition of the continental crust. *Treatise on Geochemistry*, 3, 1–64. <https://doi.org/10.1016/B0-08-043751-6/03016-4>
- Saidi, A., Brunet, M. F., & Ricou, L. E. (1997). Continental accretion of the Iran Block to Eurasia as seen from Late Paleozoic to Early Cretaceous subsidence curves. *Geodinamica Acta*, 10(5), 189–208.
- Salavati, M. (2008). Petrology, geochemistry and mineral chemistry of extrusive alkalic rocks of the Southern Caspian sea ophiolite, Northern Alborz, Iran: Evidence of alkaline magmatism in Southern Eurasia. *Journal of Applied Sciences*, 8(12), 2202–2216.
- Salavati, M., Kananian, A., & Noghreyan, M. (2013). Geochemical characteristics of mafic and ultramafic plutonic rocks in southern Caspian Sea Ophiolite (Eastern Guilan). *Arabian Journal of Geosciences*, 6, 4851–4858.
- Shafaii, M. H., Stern, R. J., Griffin, W. L., Khedr, M. Z., Kirchenbaur, M., Ottley, C. J., Whattam, S. A., Kimura, J. I., Ghorbani, G., Gain, S., O'Reilly, S. Y., & Tamura, A. (2020). Subduction initiation and back-arc opening north of Neo-Tethys: Evidence from the Late Cretaceous Torbat-e-Heydarieh ophiolite of NE Iran. *GSA Bulletin*, 132(5–6), 1083–1105.
- Shafaii Moghadam, H., Corfu, F., Chiaradia, M., Stern, R. J., & Ghorbani, G. (2014). Sabzevar Ophiolite, NE Iran: Progress from embryonic oceanic lithosphere into magmatic arc constrained by new isotopic and geochemical data. *Lithos*, 210, 224–241.
- Shaw, D. M. (1970). Trace element fractionation during anatexis. *Geochimica Et Cosmochimica Acta*, 34(2), 237–243.
- Shervais, J. W. (2022). The petrogenesis of modern and ophiolitic lavas reconsidered: Ti-V and Nb-Th. *Geoscience Frontiers*, 13(2), 101319.
- Shojaat, B., Hassanipak, A. A., Mobasher, K., & Ghazi, A. M. (2003). Petrology, geochemistry and tectonics of the Sabzevar ophiolite, North Central Iran. *Journal of Asian Earth Sciences*, 21(9), 1053–1067.
- Smith, E. I., Sanchez, A., Walker, J. D., & Wang, K. (1999). Geochemistry of mafic magmas in the Hurricane Volcanic field, Utah: Implications for small- and large-scale chemical variability of the lithospheric mantle. *The Journal of Geology*, 107(4), 433–448.
- Stampfli, G. M., & Borel, G. D. (2002). A plate tectonic model for the Paleozoic and Mesozoic constrained by dynamic plate boundaries and restored synthetic oceanic isochrons. *Earth and Planetary Science Letters*, 196(1–2), 17–33.
- Stampfli, G. M., & Kozur, H. W. (2006). Europe from the Variscan to the Alpine cycles. *Geological Society London Memoirs*, 32, 57. <https://doi.org/10.1144/GSL.MEM.2006.032>
- Stampfli, G. M., Marcoux, J., & Baud, A. (1991). Tethyan margins in space and time. *Palaeogeography Palaeoclimatology Palaeoecology*, 87(1–4), 373–409.

- Sun, S. S., & McDonough, W. F. (1989). Chemical and isotopic systematics of oceanic basalts: Implications for mantle composition and processes. *Geological Society London Special Publications*, 42(1), 313–345.
- Takahashi, E. (1986). Origin of basaltic magmas—Implications from peridotite melting experiments and an olivine fractionation model-. *Bull Volc Soc Japan Spl Issue*, 30, S17–S40.
- Temizel, I., Arslan, M., Yazar, E. A., Aslan, Z., Kaygusuz, A., & Eraydin, T. B. (2022). Zircon UPb geochronology and petrology of the tholeiitic gabbro from the Kovanlık (Giresun) area: Constraints for the Late Cretaceous bimodal arc magmatism in the Eastern Pontides Orogenic Belt NE Turkey. *Lithos*, 428, 106840.
- Thirlwall, M. F., Upton, B. G. J., & Jenkins, C. (1994). Interaction between continental lithosphere and the Iceland plume—Sr-Nd-Pb isotope geochemistry of Tertiary basalts, NE Greenland. *Journal of Petrology*, 35(3), 839–879.
- Timmerman, M. J. (2004). Timing, geodynamic setting and character of Permo-Carboniferous magmatism in the foreland of the Variscan Orogen, NW Europe. *Geological Society London Special Publications*, 223(1), 41–74. <https://doi.org/10.1144/GSL.SP.2004.223.01.03>
- Verdel, C., Wernicke, B. P., Hassanzadeh, J., & Guest, B. (2011). A Paleogene extensional arc flare-up in Iran. *Tectonics*. <https://doi.org/10.1029/2010TC002809>
- Wendt, J., Kaufmann, B., Belka, Z., Farsan, N., & Bavandpurs, A. K. (2005). Devonian/lower carboniferous stratigraphy facies patterns and palaeogeography of Iran Part II Northern and central Iran. *Acta geologica polonica*, 55(1), 31–97.
- Wensink, H., & Varekamp, J. C. (1980). Paleomagnetism of basalts from Alborz: Iran part of Asia in the Cretaceous. *Tectonophysics*, 68(1–2), 113–129.
- White, W. M., & Duncan, R. A. (1996). Geochemistry and geochronology of the Society Islands: New evidence for deep mantle recycling. *Geophysical Monograph American Geophysical Union*, 95, 183–206.
- White, W. M., & Patchett, J. (1984). Hf-Nd-Sr isotopes and incompatible element abundances in island arcs: Implications for magma origins and crust-mantle evolution. *Earth and Planetary Science Letters*, 67(2), 167–185.
- Whitney, D. L., & Evans, B. W. (2010). Abbreviations for names of rock-forming minerals. *American Mineralogist*, 95(1), 185–187.
- Winchester, J. A., & Floyd, P. A. (1977). Geochemical discrimination of different magma series and their differentiation products using immobile elements. *Chemical Geology*, 20, 325–343.
- Woodhead, J. D., Hergt, J. M., Davidson, J. P., & Eggins, S. M. (2001). Hafnium isotope evidence for 'conservative' element mobility during subduction zone processes. *Earth and Planetary Science Letters*, 192(3), 331–346.
- Zanchi, A., Zanchetta, S., Berra, F., Mattei, M., Garzanti, E., Molyneux, S., Nawab, A., & Sabouri, J. (2009). The Eo-Cimmerian (Late? Triassic) orogeny in North Iran. *Geological Society London Special Publications*, 312(1), 31–55.

Publisher's Note

Springer Nature remains neutral with regard to jurisdictional claims in published maps and institutional affiliations.

Submit your manuscript to a SpringerOpen[®] journal and benefit from:

- Convenient online submission
- Rigorous peer review
- Open access: articles freely available online
- High visibility within the field
- Retaining the copyright to your article

Submit your next manuscript at ► [springeropen.com](https://www.springeropen.com)
